Cubic AlGaN/GaN structures for device application

dem Department Physik

der Universität Paderborn

zur Erlangung des akademischen Grades eines

Doktors der Naturwissenschaften

vorgelegte

Dissertation

von

Jörg Schörmann

Paderborn, Mai 2007

Abstract

The aim of this work was the growth and the characterization of cubic GaN, cubic AlGaN/GaN heterostructures and cubic AlN/GaN superlattice structures. Reduction of the surface and interface roughness was the key issue to show the potential for the use of cubic nitrides in futur devices. All structures were grown by plasma assisted molecular beam epitaxy on free standing 3C-SiC (001) substrates.

In situ reflection high energy electron diffraction was first investigated to determine the Ga coverage of c-GaN during growth. Using the intensity of the electron beam as a probe, optimum growth conditions were found when a 1 monolayer coverage is formed at the surface. GaN samples grown under these conditions reveal excellent structural properties. On top of the c-GaN buffer c-AlGaN/GaN single and multiple quantum wells were deposited. The well widths ranged from 2.5 to 7.5 nm. During growth of $Al_{0.15}Ga_{0.85}N$/GaN quantum wells clear reflection high energy electron diffraction oscillations were observed indicating a two dimensional growth mode. We observed strong room-temperature, ultraviolet photoluminescence at about 3.3 eV with a minimum linewidth of 90 meV. The peak energy of the emission versus well width is reproduced by a square-well Poisson-Schrödinger model calculation. We found that piezoelectric effects are absent in c-III nitrides with a (001) growth direction. Intersubband transition in the wavelength range from 1.6 μm to 2.1 μm was systematically investigated in AlN/GaN superlattices (SL), grown on 100 nm thick c-GaN buffer layers. The SLs consisted of 20 periods of GaN wells with a thickness between 1.5 nm and 2.1 nm and AlN barriers with a thickness of 1.35 nm. The first intersubband transitions were observed in metastable cubic III nitride structures in the range between 1.6 μm and 2.1 μm.

List of abbreviations

AFM	*Atomic Force Microscopy*
AlGaN	*cubic* $Al_xGa_{1-x}N$
BEP	*Beam Equivalent Pressure*
CL	*Cathodoluminescence*
DAP	*Donor Acceptor Pair*
EL	*Electroluminescence*
FET	*Field Effect Transistor*
FWHM	*Full Width at Half Maximum*
GaN	*cubic GaN*
HEMT	*High Electron Mobility Transistor*
HRXRD	*High Resolution X-Ray Diffraction*
ISBT	*Intersubband transitions*
IR	*Infrared*
MBE	*Molecular Beam Epitaxy*
MOCVD	*Metal-Organic Chemical Vapor Deposition*
MQW	*Multiple Quantum Well*
PAMBE	*Plasma-assisted Molecular Beam Epitaxy*
PL	*Photoluminescence*
QCSE	*Quantum Confinement Stark Effect*
QWIP	*Quantum Well Infrared Photodetector*
SEM	*Scanning Electron Microscopy*
SL	*Superlattice*
SQW	*Single Quantum Well*
rf	*Radio Frequency*

RHEED	*Reflection High Energy Electron Diffraction*
RSM	*Reciprocal Space Map*
UHV	*Ultra High Vacuum*
UV	*Ultraviolet*
X	*Exciton*

Contents

1 Introduction **1**

2 Fundamentals **5**

2.1 Properties of III-nitrides 5

2.2 Epitaxial growth techniques 8

2.2.1 Molecular beam epitaxy 8

2.3 Characterization methods 12

2.3.1 High resolution X-ray diffraction 12

2.3.2 Atomic force microscopy 15

2.3.3 Luminescence spectroscopy 17

3 MBE of cubic GaN and cubic AlGaN **21**

3.1 *In situ* growth regime characterization of cubic GaN 21

3.1.1 Adsorption and desorption of Ga on c-GaN 21

3.1.2 Kinetic model 26

3.1.3 Growth experiments 29

3.2 Growth and characterization of cubic AlGaN/GaN heterostructures . . . 35

4 Growth of cubic AlGaN/GaN quantum wells **43**

4.1 Growth and structural properties of cubic AlGaN/GaN quantum wells . 43

4.2 Photoluminescence of cubic AlGaN/GaN quantum wells 46

5 AlN/GaN superlattices for intersubband spectroscopy **53**

5.1 Intersubband transitions 53

5.2 Growth of c-AlN/GaN superlattices 60
5.3 Structural properties of AlN/GaN SLs 64
5.4 Optical properties of AlN/GaN SLs 66

6 Conclusion **71**

7 Appendix **73**

List of Figures

2.1 Unit cell of a) the zincblende structure and b) the hexagonal structure. . 6
2.2 Different polarities in hexagonal GaN 7
2.3 Band profiles and carrier distributions in cubic and hexagonal AlGaN/GaN quantum wells; a) the cubic AlGaN/GaN DH structure and b) the hexagonal AlGaN/GaN DH structure 8
2.4 Schematic cross section of an MBE setup. 9
2.5 Schematic diagram of the RHEED diffraction geometry, showing reflection and transmission diffraction, as well as the straight-through (0,0) beam. . 10
2.6 Typical RHEED-pattern of c-GaN during growth interruption. A (2×2) reconstruction of the (-110) azimuth is observed. 11
2.7 Sketch of the diffraction geometry. The exact Bragg condition for (hkl) planes is fulfilled, if the scattering vector $\vec{Q}$ ends at a reciprocal lattice point (hkl). 13
2.8 Schematic drawing of the Phillips X´Pert MRD consisting of X-Ray tube, hybrid monochromator, Euler cradle and detector. 15
2.9 Schematic drawing of an AFM setup. 16
2.10 Schematic diagram of radiative transitions in a semiconductor; (e, h) represents intrinsic band to band, (X) free exciton,(D^0, X), (A^0, X) represents bound excitons to donator or acceptor and (D^0, h),(h, A^0) free to bound, (D^0, A^0) donor to acceptor transitions. 18
2.11 Schematic diagram of the photoluminescence setup. 19

3.1 a) A sketch of the sample structure with the RHEED geometry. b) A (2×2) reconstruction of a c-GaN surface during growth interruption. The red rectangle indicates the area where the RHEED intensity was recorded. 22

3.2 The intensity of a reflected high energy electron beam (RHEED intensity) versus time measured during the evaporation of Ga onto c-GaN at a substrate temperature of $T_S = 720°C$. The Ga-fluxes are indicated. The spectra are normalized to one and vertically shifted for clarity. 23

3.3 RHEED intensity transient for a Ga-flux of $F_{Ga} = 4.3 \times 10^{14}\ cm^{-2}s^{-1}$ and $7.5 \times 10^{14}\ cm^{-2}s^{-1}$. 24

3.4 RHEED intensity transients for Ga-fluxes of $4.3 \times 10^{14}\ cm^{-2}s^{-1}$ and $7.5 \times 10^{14}\ cm^{-2}s^{-1}$. After a transition time Δt_k a kink in the transients is observed. The estimated Ga-coverage is plotted on the right side. 25

3.5 RHEED intensity transients for a Ga-flux of $2 \times 10^{14} cm^{-2}s^{-1}$. The red curves show the simulations for a flux of $2 \times 10^{14}\ cm^{-2}s^{-1}$ and three different desorption fluxes as indicated in the figure. Good agreement was achieved for a desorption flux of $1.6 \times 10^{14}\ cm^{-2}s^{-1}$. 27

3.6 RHEED intensity transients for two Ga-fluxes together with simulations as indicated in the figure. Good agreement was achieved within the linear decrease of the RHEED intensity. 28

3.7 RHEED intensity transients measured during the growth of c-GaN, which started after opening the N source. The RHEED intensity measured during growth shows the amount of excess Ga (indicated in the figure) on the c-GaN surface. Ga-fluxes are 4.4×10^{14}, 3.2×10^{14} and $1.2 \times 10^{14}\ cm^{-2}s^{-1}$ for the coverages of 1, 0.8, and 0 ML, respectively. 29

3.8 Root-mean-square (RMS) roughness of c-GaN layers measured by $5 \times 5\mu m^2$ scans vs. Ga-flux during growth. The corresponding values of the Ga-coverage during growth are also included. Minimum roughness is obtained with an excess coverage of 1 ML. The line is added for better overview. 30

3.9 $\omega - 2\Theta$ scan of the (002) reflex of sample 1287. The inset shows the ω-scan of this sample revealing a FWHM of 16 arcmin. 31

3.10 Full width at half maximum (FWHM) of c-GaN layers vs. Ga-flux during growth. The corresponding values of the Ga-coverage during growth are also included. Minimum linewidth is obtained with an excess coverage of 1 ML. The line is a guide for the eyes. 32

3.11 Line width of rocking curve (FWHM) of the (002) reflex of cubic GaN epilayers grown on 3C-SiC(001) substrates versus thickness of the GaN epilayers. 34

3.12 Schematic sketch of an AlGaN/GaN heterostructure 35

3.13 RHEED intensity measured during initial growth of $c - Al_{0.25}Ga_{0.75}N$. The RHEED intensity after opening the N shutter yields the amount of excess Ga on the c-GaN surface. After opening the Al shutter RHEED intensity oscillations are observed indicating a two-dimensional growth mode with a rate of 177 nm/h. 37

3.14 Reciprocal space map of the c-GaN (-1-13) reflex of sample 1117. The c-AlGaN layer is pseudomorph to the c-GaN buffer layer. The Al-mole fraction is x=0.3 38

3.15 Reciprocal space map of the c-GaN (-1-13) reflex of sample 1360. The c-AlGaN layer is relaxed to the c-GaN buffer layer. The Al-mole fraction is x=0.7 39

3.16 XRD rocking curve of the (002) reflex of sample 1117. The full width at half maximum of the c-GaN and the c-AlGaN layer are nearly identical. . 40

3.17 Relation between the Al mole fraction x of c- $Al_xGa_{1-x}N$ and the ratio of Al-flux to the total metal flux for films grown under 1ML Ga-coverage. The mole fraction x was determined by HRXRD. 41

3.18 RMS surface roughness of different c-$Al_xGa_{1-x}N$/GaN heterostructures with an Al mole fraction between x=0 and x=1. Layers were grown with a 1 ML Ga coverage. The line is a guide for the eyes. 42

4.1 Schematic Sketch of a multiple quantum well structure 44
4.2 Measured $\omega - 2\Theta$ scan of a 15-fold $Al_{0.3}Ga_{0.7}N$/GaN structure (solid line) and simulated data (dotted line). The well and the barrier width are 3 nm and 6 nm. 45
4.3 Reciprocal space map around the asymmetric (-1-13) reflex of sample 1372. The quantum wells are pseudomorph to the c-GaN buffer. 46
4.4 Room temperature photoluminescence of cubic $Al_{0.15}Ga_{0.85}N$/GaN single and multiple quantum well structures. The QW transition energy is E=3.30 eV and the linewidth is 90 meV for the SQW and 103 meV for the MQW. 47
4.5 Low temperature photoluminescence of cubic $Al_{0.15}Ga_{0.85}N$/GaN SQW and MQW structures. The QW transition energy is E=3.33 eV and 3.35 eV and the linewidth is 64 meV and 80 meV, respectively 48
4.6 Schematic view of a quantum well without and with built-in field. Electrons and holes are localized in opposite corners leading to a red-shift of the lowest transition and to a reduction of the oscillator strength compared to the flat band case in the cubic system [53]. 49
4.7 Energy difference of cubic and hexagonal AlGaN/GaN QWs as a function of well width [54]. The full curve for the cubic QWs was calculated using the self-consistent Poisson-Schrödinger model [55]. The hexagonal QWs show a red-shift of the transition energy below the band gap of hexagonal GaN. 50

5.1 Schematic sketch of an intersubband transition in the conduction band after absorption of a photon with equal energy to the difference between the ground state E_0 and the first excited state E_1 [70]. 54
5.2 The (a) bound-to-bound, (b) bound-to-quasi-bound and (c) bound-to-continuum transitions of electrons in the conduction band are depicted. . 55
5.3 Band gap of $Al_xGa_{1-x}N$ and the conduction band offset of $GaN/Al_xGa_{1-x}N$ as a function of the Al mole fraction. 56

5.4 Schematic sketch of transitions in quantum wells with different well thicknesses. The blue curve indicates case (a) the red curve case (b) and the green curve case (c) [70]. 57

5.5 Typical quantum well design structure with two bound states. Quantum wells are shown without bias voltage on the left side and with applied bias voltage on the right side. 58

5.6 Mesa structure of a typical quantum well infrared photo detector. A bias voltage is supplied and a photocurrent is measured. 59

5.7 Transition energies of AlN/GaN multiple quantum well versus the QW thickness calculated by a self-consistent Poisson-Schrödinger model. . . . 60

5.8 Schematic sketch of an AlN/GaN MQW structure for intersubband transitions. The thicknesses of the wells vary between 1.3 and 1.9 nm, the thickness of the barriers is 1.5 nm. 61

5.9 RHEED timescan of sample 1518 on an extended scale. The shutter sequence and the coverage of 1 ML during c-GaN growth is indicated in the figure. 62

5.10 RHEED intensity versus time during the growth of an AlN/GaN superlattice of sample 1518. The Fig. shows the RHEED intensities of period 2 and 3 and of period 18 and 19. The shaded area indicates the growth of the individual layer. The scans are vertically shifted for clarity. 63

5.11 ω-2Θ scan and simulated data of the (002) reflex of sample 1518. The sample consists of a 20-fold AlN/GaN MQW structure. The simulation reveals a barrier thickness of 1.35 nm and a QW thickness of 1.75 nm. . . 64

5.12 An SEM image of a waveguide with approximately 2 mm width and 5 mm length [70]. 66

5.13 Illustration of light propagating through a waveguide. 66

5.14 Room-temperature absorbance spectra of 4 AlN/GaN MQW structures and of a substrate. Absorption was observed in the range of 0.6 eV to 0.8 eV (1.6 μm to 2 μm). The spectra are vertically shifted for clarity. 67

5.15 Intersubband absorption of four AlN/GaN MQWs. The spectra are plotted after subtraction of the substrate background in the spectral range between 0.5 eV and 1.1 eV (1.1 μm and 2.5 μm). A shaded area indicates the wavelength of 1.55 μm. The FWHM of all samples is about 200 meV. 68

5.16 Simulation of the conduction band of sample 1518. Two bounded states are observed within the quantum well. The shaded area indicates the distribution of the first excited state E_1. 69

5.17 Transition energies of AlN/GaN multiple quantum wells versus the QW thickness as shown in Fig. 5.7. The experimental data show good agreement with the calculated data. 70

1 Introduction

In the last decade, the group III-nitrides AlN, GaN, InN and their alloys have become one of the most important classes of semiconductor materials. In particular, GaN and Ga-rich $In_xGa_{1-x}N$, and $Al_xGa_{1-x}N$ thin films are used in a variety of commercial optoelectronic devices, including green and blue light emitting diodes (LEDs) and lasers [1]. By combining UV-emitting GaN LEDs with phosphor it is possible to fabricate high efficiency white light emitters which are predicted to play a crucial role in future high-efficiency home and commercial lighting systems [2]. Group III-nitrides have also found application in other electronic devices. For example, advanced GaN/AlGaN high-power microwave transistors are now commercially available.

Group III-nitrides crystalize in the stable wurtzite (hexagonal) structure or in the metastable zinc blende (cubic) structure. An important difference between these material modifications is the presence of strong internal electrical fields in hexagonal III-nitrides grown along the polar (0001) c-axis, while these "built-in" fields are absent in cubic III-nitrides.

These "built-in" polarization-induced electric fields limit the performance of optoelectronic devices which employ quantum well active regions. Especially the spatial separation of the electron and hole wave functions caused by the internal fields reduces the oscillator strength of transitions and limits the recombination efficiency of the quantum wells [3]. To solve this problem, much attention has been given to the growth of wurtzite structures with nonpolar orientations, e.g., growth along the a, m and R directions [4][5][6].

Because of their higher crystallographic symmetry cubic nitrides grown in (001) direction

offer an alternative way to produce nitride based quantum structures that are unaffected by internal polarization fields. The zinc blende III-N are metastable and can only be grown in a very narrow window of process conditions [7]. However, the use of nearly lattice matched, freestanding high quality 3C-SiC substrates led to substantial improvements of the crystal quality of c-III nitrides [8].

Group III-nitrides are usually grown by two different techniques, either metal-organic chemical vapor deposition (MOCVD) or molecular beam epitaxy (MBE). All samples included in the present work were grown by plasma-assisted molecular beam epitaxy (PAMBE) where the chemically inert nitrogen molecule is activated by a plasma discharge.

As an important step to further improve the c-GaN surface morphology in a systematic way, it is essential to understand the surface structure and the underlying growth process on an atomic scale. Investigations of the impact of growth temperature and surface stoichiometry on epilayer deposition are the strength of MBE due to its *in situ* tools, such as reflection high energy electron diffraction (RHEED). This technique has become extremely valuable for the understanding of growth mechanisms of thin films.

The present work is structured in five main parts. A short introduction is given in chapter 1. In the first part of chapter 2 the basic properties of III-nitrides especially the difference between hexagonal GaN grown along the (0001) direction and cubic GaN grown along the (001) direction are summarized. In the second part of chapter 2 the growth technique (molecular beam epitaxy, MBE) and the characterization methods used for this work are described. Chapter 3 gives an overview of the structural properties (dislocation density, roughness) of c-GaN and c-AlGaN. The growth of these structures was optimized using reflection high energy electron diffraction (RHEED) as an *in situ* control method. Optimum growth conditions were achieved using a well defined Ga coverage during c-GaN epitaxy. Chapter 4 describes the growth and the properties of c-AlGaN/GaN Quantum Wells (QWs). These structures find their application as ultraviolet emitters in the 250 nm to 400 nm range. AlN/GaN superlattices can be used as infrared detectors in the 1 μm to 3 μm range. The growth of AlN/GaN superlattices as well as their structural and optical properties are described in chapter 5. First intersubband transitions in the

near infrared region were observed with c-III-nitrides. Finally the conclusions are given in chapter 7.

2 Fundamentals

This chapter begins with a brief introduction of the most important differences between hexagonal and cubic structures. Firstly, the impact of the huge spontaneous and piezoelectric polarization fields on radiative recombination from quantum wells is discussed. Secondly, a description of the molecular-beam epitaxy (MBE) system used for growth is given followed by a description of the characterization methods which have been used.

2.1 Properties of III-nitrides

Group III-nitrides crystallize in the stable hexagonal (wurtzite) structure or in the metastable cubic (zincblende) structure. Figure 2.1 shows a ball-and-stick model of these two structures. The unit cell of the cubic and the hexagonal structure is shown in Fig. 2.1 a) and b).

In both cases, each group-III atom is tetrahedrally coordinated to four nitrogen atoms. The main difference between these two structures is the stacking sequence of closed packed diatomic planes. The stacking sequence is ABABAB along the wurtzite (0001) direction and ABCABC along the zincblende (111) direction.
Due to non-centro-symmetric configuration and ionic binding, the hexagonal nitrides exhibit large piezoelectric effects under strain along the c-direction and spontaneous polarization at hetero-interfaces. The genesis of the polarization is two-fold: the piezoelectric effects and the difference in spontaneous polarization between AlN, GaN, and InN even in the absence of strain.

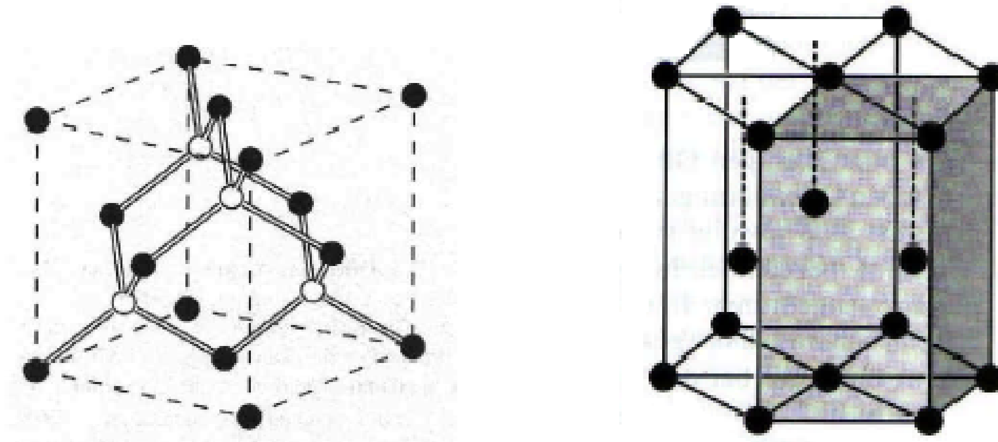

Figure 2.1: Unit cell of a) the zincblende structure and b) the hexagonal structure.

Polarization depends on the polarity of the crystal, namely whether the bonds along the *c*-direction are from cation (Ga) sites to anion (N) sites or vice versa. As can be seen in Fig. 2.2, the basal surface of GaN is either Ga-faced or N-faced (also known as Ga-polarity and N-polarity), which means that the top position of a [0001] surface is either gallium or nitrogen, respectively.

The polarity of the crystal gives rise to an internal electric field due to the interaction between Ga cation and N anion, which is called polarization field. If strain exists in the system, it will modify the electric field by changing the spacing between the Ga plane and the N plane. This strain-induced additional electric field is called piezoelectric field. On the contrary, zincblende (cubic) GaN has a symmetric configuration along the (001) growth direction, where the polarization fields are absent.
Due to the polarization field difference in GaN and InGaN, or GaN and AlGaN, band diagram and carrier distribution will be influenced by these electric fields. In the case of AlGaN/GaN quantum wells, the band profile and carrier distribution difference in the cubic and hexagonal configuration is shown in Fig. 2.3 a) and b).

In hexagonal AlGaN/GaN the polarization field in AlGaN and GaN wells results in a net electric field E_{GaN}, which makes the tilt of the GaN energy gap in the band profile

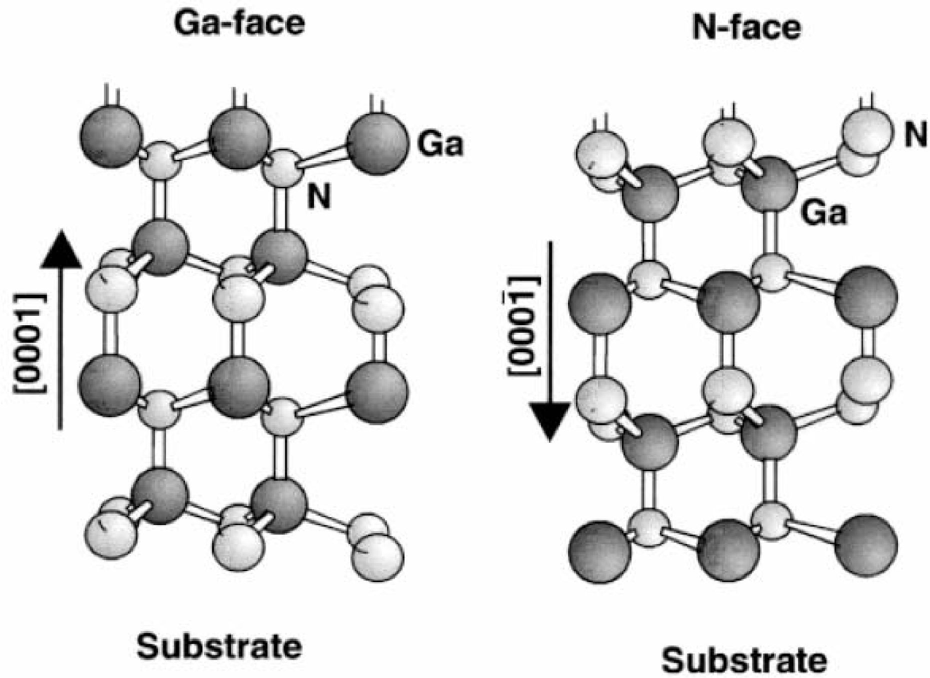

Figure 2.2: Different polarities in hexagonal GaN

and separates the electron and holes to the two opposite sides of the well. This results in a lower transition energy of the electron from the conduction band to the valence band. The wave function overlap also decreases with increasing well thickness. This effect degrades the emission intensity with increasing the well thickness. Both effects are called the quantum confinement Stark effect (QCSE). *Bai et al.* have studied the dependency of PL intensity with the well thickness [9]. They found that the PL intensity decreases monotonically with the well thickness. The intensity will totally quench with a well thickness above 5 nm. The optimum GaN well thickness in h-AlGaN/GaN multiple quantum wells is 2-3 nm [1] [10]. Chichibu *et al.* have shown that the polarization field is inactive in cubic polytypes by time-integrated and time-resolved PL measurements on cubic InGaN/GaN MQWs [11]. The same properties described above also apply to InGaN/GaN quantum wells. Therefore it can be expected that cubic III-nitrides will have a different PL intensity dependence on the well thickness, which is an advantage for the fabrication of cubic III-nitride based devices.

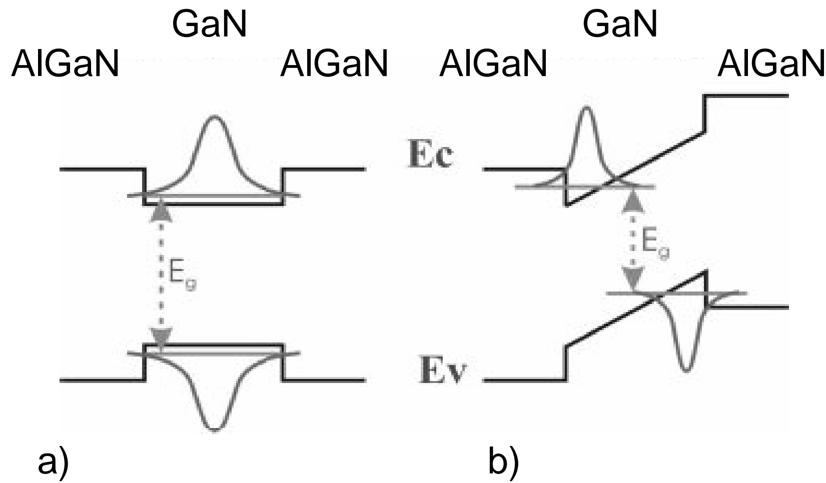

Figure 2.3: Band profiles and carrier distributions in cubic and hexagonal AlGaN/GaN quantum wells; a) the cubic AlGaN/GaN DH structure and b) the hexagonal AlGaN/GaN DH structure

2.2 Epitaxial growth techniques

Group III-nitrides are usually grown by two different techniques, either metal-organic chemical vapor deposition (MOCVD) or molecular beam epitaxy (MBE). In the following the MBE growth process will be reviewed to provide the reader with an understanding of this growth process which relate on the materials under investigation.

2.2.1 Molecular beam epitaxy

Molecular beam epitaxy (MBE) is an advanced deposition technique which is performed in ultra-high vacuum. With MBE, atoms are delivered to a substrate through an ultra-high vacuum atmosphere ($< 10^{-9} mbar$). This atmosphere allows the atoms to reach the substrate without colliding with other atoms or molecules. The heated substrate surface allows the arriving atoms to arrange themselves across the surface forming an almost perfect crystal structure. Through the use of shutters and precise control of the effusion

cell temperatures almost any material composition and doping can be achieved.
All cubic III-nitride structures used for this work were grown by MBE in a *Riber 32* system equipped with an *Oxford Applied Research HD25* radio frequency plasma source for activated nitrogen atoms. Figure 2.4 shows a schematic sketch of our MBE system.

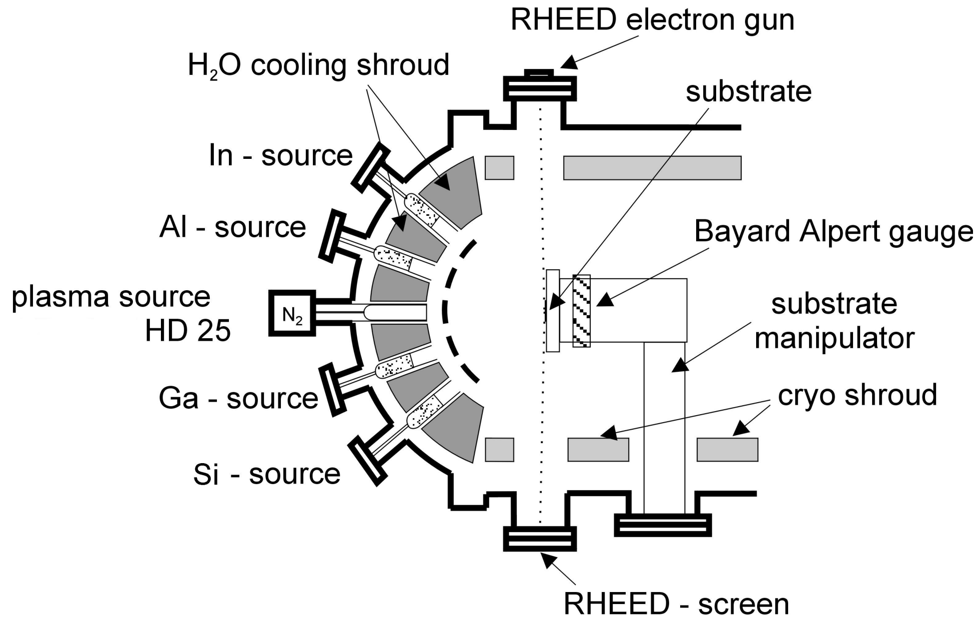

Figure 2.4: Schematic cross section of an MBE setup.

A liquid nitrogen-cooled shroud is used to enclose the entire growth area in order to minimize any residual vapor in the vacuum chamber during growth. To improve the uniformity of the layer deposition, the substrate holder can be rotated. A Bayard-Alpert gauge mounted on the back of the substrate manipulator is used to measure the beam equivalent pressure (BEP) of the element species in the effusion cells. The MBE is equipped with 4 *ABN 35* standard effusion cells which are used for the evaporation of Ga, Al, In and Si. The temperatures of these cells are measured by thermocouples at the bottom of a pyrolytic boron nitride (PBN) crucible. The purity of the source material is 99.9999 %. The plasma source for activated nitrogen atoms is water-cooled and operates with an inductive coupled radio frequency (RF) of 13.65 MHz at 130-260 W. Typical flow rates of the N_2 gas were 0.2-0.4 sccm, resulting in N-background pressure of about $2 \cdot 10^{-5}$ mbar. More details about MBE are given in Ref. [12].

A significant part of nitride growth by MBE is the ability to monitor the growing surface *in situ* using Reflection High Energy Electron Diffraction (RHEED). RHEED is limited to high vacuum conditions which restricts its use for other growth techniques, e.g. MOCVD. A high energy electron beam (10-20 keV acceleration voltage) is directed at a grazing angle (1-2°) onto the substrate surface. The diffracted beam is forward-scattered to a fluorescence screen. The resulting diffraction pattern on this screen is a superposition of the contribution of electrons that have been scattered from atomically flat regions of the crystal and those that have been transmitted through asperities rising above the surface. Thus, the formed diffraction pattern gives information about the symmetry and periodicity of ordered layers near the surface and the position of atoms within the unit cell. Figure 2.5 shows a schematic diagram of the RHEED diffraction geometry showing reflection (2D) and transmission (3D), as well as the straight-through or (0,0) beam.

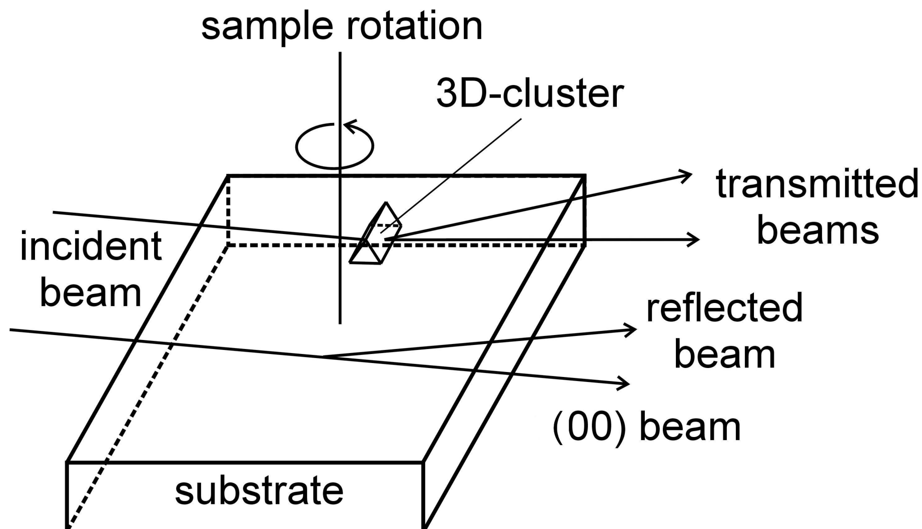

Figure 2.5: Schematic diagram of the RHEED diffraction geometry, showing reflection and transmission diffraction, as well as the straight-through (0,0) beam.

The observed RHEED-pattern can be used to monitor the growth dynamics in real time. RHEED is therefore capable of measuring intensity oscillations of the diffraction pattern. These RHEED intensity oscillations can be measured on the specular reflected

spot in the RHEED-pattern. In our case RHEED intensity oscillations were used to measure the growth rate of c-AlGaN and c-AlN. Furthermore, the in-plane lattice parameter of the growing surface can be determined. Figure 2.6 shows a typical RHEED-pattern of a c-GaN surface. The pattern shows a (2×2) reconstruction during growth interruption.

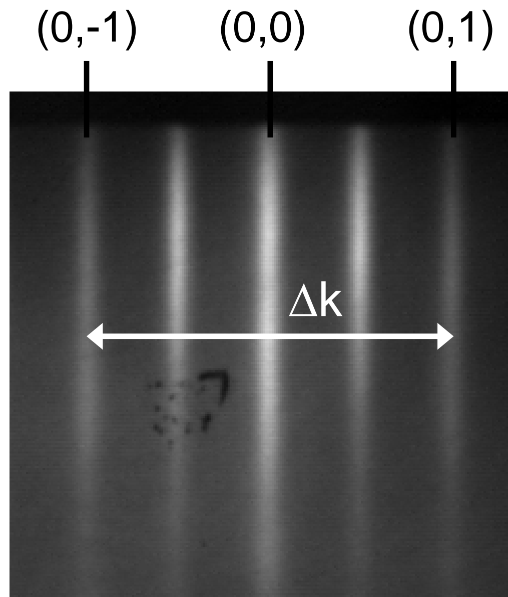

Figure 2.6: Typical RHEED-pattern of c-GaN during growth interruption. A (2×2) reconstruction of the (-110) azimuth is observed.

The distance Δk between the (0,-1) and the (0,1) reflex is inverse proportional to the in-plane lattice parameter of the growing layer. This offers the possibility to measure the distance Δk quasi continuously during growth. Therefore this technique enables the *in situ* study of the relaxation process of strained epilayers on lattice mismatched substrates. Details about RHEED are given in [13].

Using the reflected high energy electron beam as a probe, we developed a method which allows to measure the Ga-coverage of the GaN surface during growth with submonolayer accuracy. Details are given in chapter 3.

2.3 Characterization methods

2.3.1 High resolution X-ray diffraction

High resolution X-ray diffraction (HRXRD) is a powerful tool for the non-destructive *ex situ* investigation of epitaxial layers, heterostructures and superlattice systems. The information obtained from diffraction patterns concerns the composition and uniformity of epitaxial layers, their thickness, the built-in strain, the strain relaxation and the crystalline perfection related to their dislocation density.
For a single crystal the diffraction of X-rays can be described by the Bragg equation [14].

$$\lambda = 2 \cdot d_{hkl} \cdot \sin\Theta \tag{2.1}$$

The triplet (hkl) denotes the Miller indices, and d_{hkl} is given by

$$d_{hkl} = \frac{a_0}{\sqrt{h^2 + k^2 + l^2}} \tag{2.2}$$

d_{hkl} is the spacing of the lattice planes, a_0 is the lattice constant, λ is the wavelength of the X-ray radiation and Θ is the incident angle of the radiation. Details of X-ray diffraction can be found in references [15], [16], [17].

It is a convenient and common way to describe X-ray diffraction in reciprocal space. The reciprocal lattice is formed by the terminal points of reciprocal repetition vectors $\vec{b_1}$, $\vec{b_2}$ and $\vec{b_3}$ which are related to the primitive vectors of crystal lattice $\vec{a_1}$, $\vec{a_2}$ and $\vec{a_3}$ by:

$$\vec{b_i} = 2 \cdot \pi \cdot \frac{\vec{a_j} \times \vec{a_k}}{\vec{a_1} \cdot (\vec{a_2} \times \vec{a_3})} \qquad i, j, k \ \ cycl. \tag{2.3}$$

In reciprocal space the plane with the Miller indices (hkl) is described by the reciprocal vector which is given by

$$\vec{G_{hkl}} = h \cdot \vec{b_1} + k \cdot \vec{b_2} + l \cdot \vec{b_3} \tag{2.4}$$

The condition of diffraction in equation 2.1 by the plane (hkl) can be transferred in reciprocal space (see for example [15]) in the form:

$$\vec{Q} = \vec{G_{hkl}} \tag{2.5}$$

$\vec{Q}$ is the scattering vector defined as $\vec{Q} = \vec{k_\varepsilon} - \vec{k_\delta}$ where $\vec{k_\varepsilon}$ and $\vec{k_\delta}$ are the wave vectors of incident and diffracted waves as indicated in Fig. 2.7.

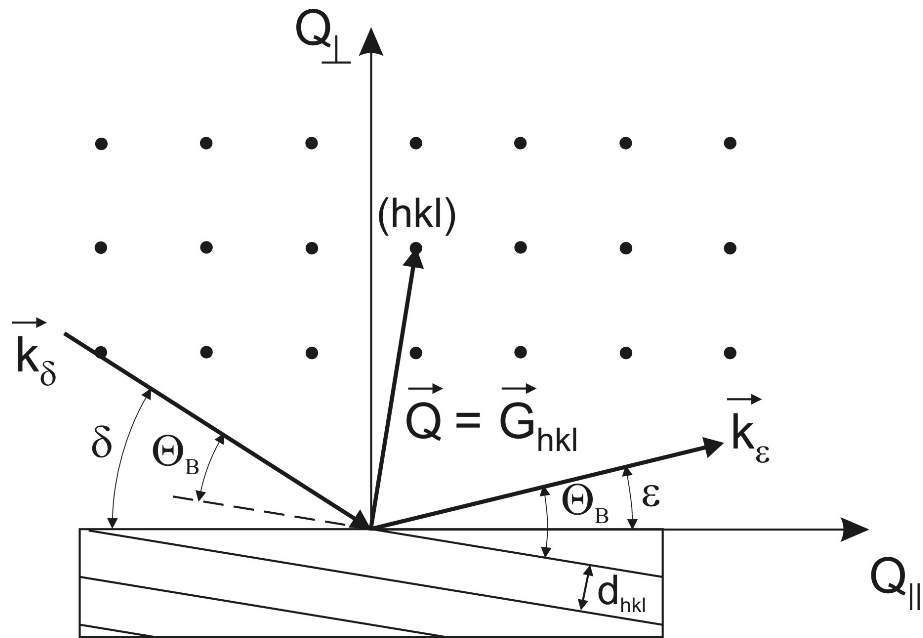

Figure 2.7: Sketch of the diffraction geometry. The exact Bragg condition for (hkl) planes is fulfilled, if the scattering vector $\vec{Q}$ ends at a reciprocal lattice point (hkl).

Thus, in reciprocal space the diffraction plane is represented as a reciprocal lattice point and the diffraction geometry defined by the incident and by the detection angles is represented by the scattering vector. When the scattering vector ends at a reciprocal lattice point (hkl) the exact Bragg condition is fulfilled. Scattered X-ray intensity around a reciprocal lattice point (RLP) is strongly influenced by the structural properties of the crystalline material. Therefore the measurements and detailed analysis of diffracted intensity around reciprocal lattice points is the subject of high resolution diffractometry.

The variation of the incident beam allows to analyze different crystal properties. Three types of measurements are performed: $\omega - 2\Theta$ scans, ω scans and two dimensional intensity distributions in reciprocal space, e.g. Reciprocal Space Maps (RSM).

- $\omega - 2\Theta$ scans

  This kind of scan allows measurements where the angular rotation speed of the detector is twice that of the incident angle. The detector angle moves along a reciprocal lattice vector. With this kind of scan geometry it is possible to get information on lattice parameter and chemical composition of epitaxial layers.

- ω scans

  In this configuration the detector angle is fixed and the sample is rotated. In symmetrical scan geometry the ω scan is perpendicular to a $\omega - 2\Theta$ scan if one describes this in reciprocal space. Using ω scans, also called rocking curve, it is possible to get information about the layer quality and the dislocation density [32].

- Reciprocal Space Maps (RSM)

  A RSM is a combination of ω scans and $\omega - 2\Theta$ scans. The result is a two dimensional distribution of intensity in reciprocal space. Using different kinds of measurements it is possible to get information about the strain status and the chemical composition.

For this work, a *Phillips X´Pert Diffractometer* was used with a copper anode emitting the K_{α_1} radiation of $\lambda = 1.54056$ $\mathring{A}$ and the K_{α_2} radiation of $\lambda = 1.54444$ $\mathring{A}$. The tube is equipped with a line focus and a hybrid monochromator, which guarantees a beam divergence of 47 arcsec. The monochromator consists of a graded parabolic mirror in connection with a (220) channel-cut Germanium crystal. The mirror parallelizes the beam and the Germanium crystal blocks the K_{α_2} line. The samples are mounted onto an Euler cradle which allows an independent variation of the angle of incident ω, the diffraction angle 2Θ, the rotation around the surface normal ϕ and the incident axis ψ, as well as a linear motion in the three directions x, y and z. A schematic sketch of the diffractometer is shown in Fig. 2.8.

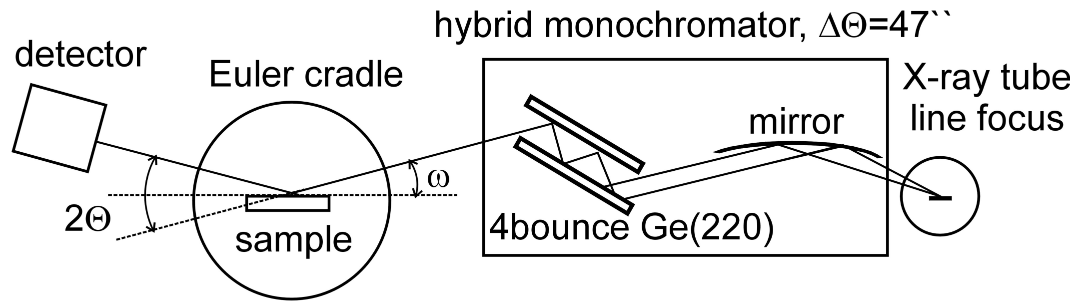

Figure 2.8: Schematic drawing of the Phillips X´Pert MRD consisting of X-Ray tube, hybrid monochromator, Euler cradle and detector.

The measurements were performed in double axis configuration using a $\frac{1^\circ}{16}$ slit in front of the detector resulting in a resolution of 1.8 arcmin. Another configuration is the so called triple axis configuration where a second (220) Germanium crystal is placed in front of the detector. The resolution in triple axis configuration is 0.084 arcmin.

2.3.2 Atomic force microscopy

Atomic force microscopy (AFM) offers a way to get information about the surface morphology of epitaxial layers. This method allows measuring the surface roughness on an atomic scale.
Figure 2.9 shows the schematic diagram of an AFM setup. A tip consisting of SiN is mounted at the end of a cantilever.

The tip is moved towards the investigated surface so that only atomic forces are relevant. The tip is approached to the surface by piezoelements and then starts scanning the surface. The distance between the tip and the surface will be held constant by theses piezoelements and an optical measurement yields the height profile. A laser beam is focused on top of the tip where it is reflected and detected with a photo diode which is sensitive to changing positions. If the tip is linked during scanning the position of the laser beam on the photo diode will change. The amplitude is proportional to the surface morphology.

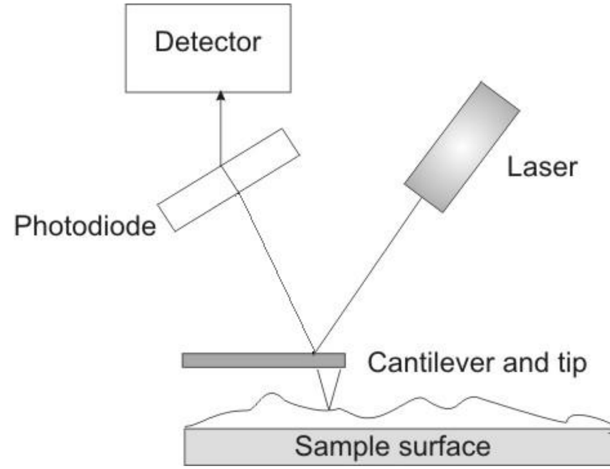

Figure 2.9: Schematic drawing of an AFM setup.

Surface Roughness

A quantity for the roughness is the so-called Root Mean Square (RMS) roughness. The RSM in one dimension is defined as

$$RMS = \left[\frac{1}{L} \int_0^L (z(x) - \bar{z})^2 \cdot dx \right]^{\frac{1}{2}} \tag{2.6}$$

where L is the scan width, z(x) the line profile and $\bar{z}$ is the median value of the height. However, the roughness is not determined in real space, it is determined via Fourier transformation in frequency space. In frequency space the RMS is

$$RMS = \left[\int_{f_1}^{L_2} P(f) \cdot df \right]^{\frac{1}{2}} \tag{2.7}$$

P is the power spectral density, which is defined as the square of the Fourier transformed line profile. For the line profile z(x) follows

$$P(f) = \frac{1}{L} \left| \int_0^L e^{-i \cdot 2 \cdot \pi \cdot f \cdot x} \cdot z(x) \cdot dx \right|^2 \tag{2.8}$$

As the topography of the scanned area is 2-dimensional and consists of discrete data

points the power spectral density in two dimensions is calculated by the Fast-Fourier Transformation (FFT) [18].

2.3.3 Luminescence spectroscopy

Luminescence is the emission of electromagnetic radiation in excess of thermal radiation. In general the high energy part of the spectrum is determined by the gap energy of the semiconductor. Excitation of the luminescent material is necessary to achieve radiative recombination of excess carriers. The luminescence is specified according to the mode of excitation. Three types of excitation for semiconductors are listed below.

- Photoluminescence (PL), excited by incident photons, e.g. a LASER
- Cathodoluminescence (CL), excited by incident electrons, e.g. a scanning electron microscope which allows position-sensitive measurements.
- Electroluminescence (EL), excited by application of an electric field, e.g. a power supply

After excitation the carriers in the semiconductor are in a non-equilibrium state. To achieve thermal equilibrium carrier recombination processes have to occur and radiative recombination results in light emission. Different optical properties can be observed [19] [20] [21]. In bulk semiconductors different kinds of optical transitions are present. In films of high purity, e.g. intrinsic semiconductor band to band (e,h) and free exciton (X) transitions are dominating. A schematic drawing of the various radiative recombination processes leading to emission in semiconductors is shown in Fig. 2.10.

The most common radiative transitions in c-GaN are described below and for example in references [22], [23], [24], [25].

Band to band (e, h) transitions are described by the difference of the conduction and the valence band edges where an electron from the conduction band recombines with a hole in the valence band.

The free exciton transition (X) is important in photoluminescence and is a typical indica-

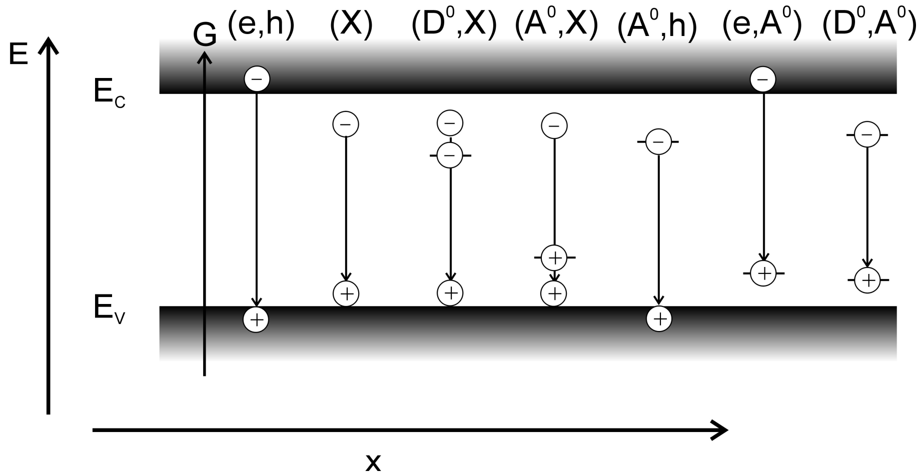

Figure 2.10: Schematic diagram of radiative transitions in a semiconductor; (e, h) represents intrinsic band to band, (X) free exciton,(D^0, X), (A^0, X) represents bound excitons to donator or acceptor and (D^0, h),(h, A^0) free to bound, (D^0, A^0) donor to acceptor transitions.

tor for a high sample quality. In case of a high-purity semiconductor the Coulomb interaction between the generated electron and hole can bind them into the quasi-hydrogenic exciton. High doping or defect levels can reduce the probability of exciton formation, because the free charges tend to screen out the Coulomb interaction.
Donor to acceptor transition (D^0, A^0) occurs when a semiconductor is doped or an impurity related level is introduced. According to the hydrogen model the binding energy E_D (E_A) of the electron (hole) to the donor (acceptor) impurity can be estimated with the effective mass approximation.
The PL setup used for this work enables the realization of temperature- and intensity-dependent measurements. A sketch of the PL setup is given in Fig. 2.11.

The luminescence was excited by the 325 nm (3.81 eV) line of a continuous-wave single-mode HeCd laser with an output power of about 4 mW. The laser plasma lines were suppressed by an interference filter. The laser light was then focussed onto the mirror reflecting the light onto the sample. The PL signal was dispersed by a grating monochromator and detected using a GaAs photomultiplier and a photon counting sys-

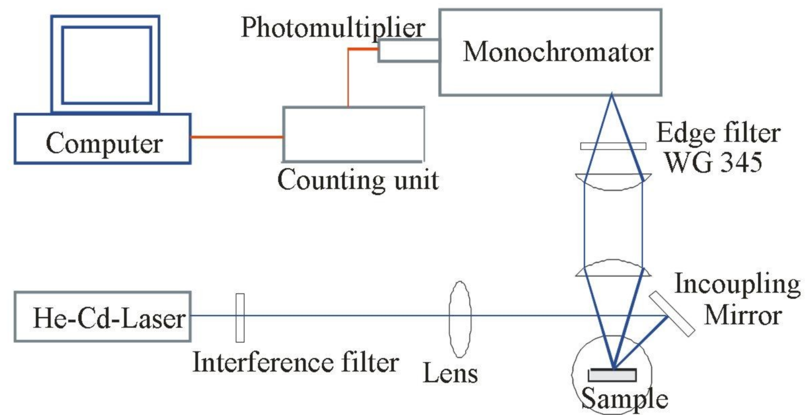

Figure 2.11: Schematic diagram of the photoluminescence setup.

tem. A computer system served for data collection and visualization. A He bath cryostat allowed temperature-dependent measurements in the range from T=2 - 300 K.

3 MBE of cubic GaN and cubic AlGaN

In this chapter, the synthesis of cubic GaN layers on free standing 3C-SiC (001) substrates is discussed. These layers serve as buffer for subsequent growth of heterostructures and quantum structures. Hence, the simultaneous accomplishment of a high morphological and structural quality of the GaN layer is required in order to realize heterostructures with smooth interfaces and low dislocation densities.

3.1 In situ growth regime characterization of cubic GaN using reflection high energy electron diffraction

3.1.1 Adsorption and desorption of Ga on c-GaN

As an important step to improve the c-GaN surface morphology in a systematic way, it is essential to understand the underlying growth process on an atomic scale. In particular, the kinetics of adsorption and desorption on the surface are considered as key parameters that govern the surface morphology, incorporation kinetics and consecutively the overall material quality. In molecular beam epitaxy of hexagonal GaN, two-dimensional surfaces are commonly achieved under slightly Ga-rich conditions with theoretical [26] and experimental [27], [28] evidences suggesting that the growth front is stabilized by a metallic adlayer. The optimum growth conditions for the epitaxial growth of c-GaN are mainly determined by two parameters, the surface stoichiometry and the substrate temperature [7]. Both parameters are interrelated; therefore an *in situ* control of substrate

temperature and surface stoichiometry is highly desirable. The study of the surface reconstruction by RHEED was one of the key issues in understanding the c-III-nitride growth [7], [22], [29]. First principle calculations by Neugebauer et al. [30] show that all energetically favoured surface modifications of the nonpolar (001) c-GaN surface are Ga stabilized and therefore optimum growth conditions are expected under slightly Ga-rich conditions. It is shown quantitatively that a 1 monolayer (ML) Ga-coverage favours two-dimensional growth and yields c-GaN layers with a minimum surface roughness [31]. Cubic GaN layers used for the RHEED experiments were grown under Ga-rich condi-

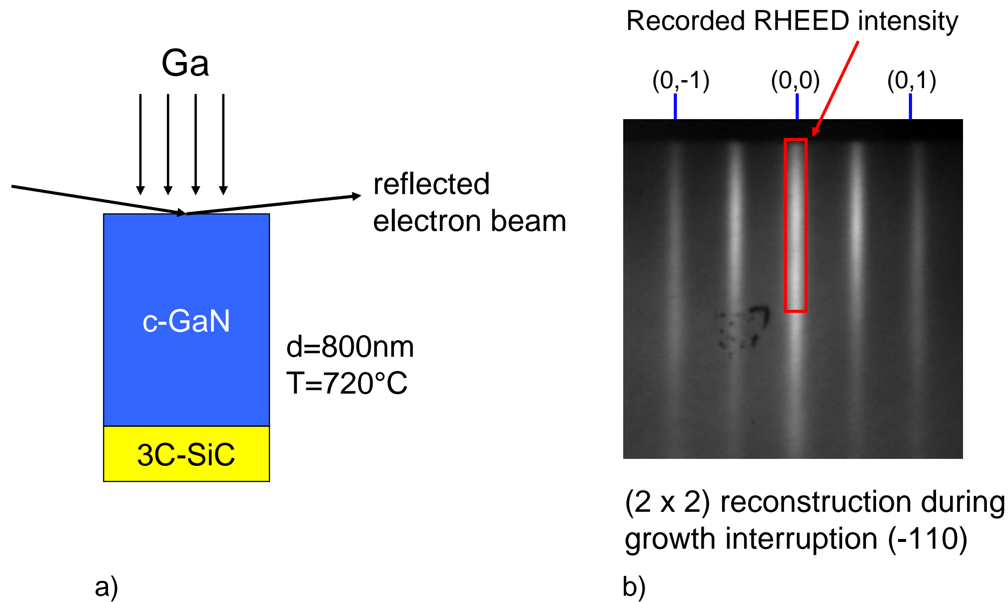

Figure 3.1: a) A sketch of the sample structure with the RHEED geometry. b) A (2×2) reconstruction of a c-GaN surface during growth interruption. The red rectangle indicates the area where the RHEED intensity was recorded.

tions [32] on 3C-SiC (001) substrates [33]. The substrates were chemically etched and backcoated with silicon for efficient heat incoupling. Prior to growth the substrates were subjected to an Al deoxidation process at $T_S = 800°C$ using Al BEP of 8×10^{-8} mbar in order to remove native oxides. The substrate temperature during growth was kept constant at $T_S = 720°C$. The adsorption and desorption of metal Ga layers on the

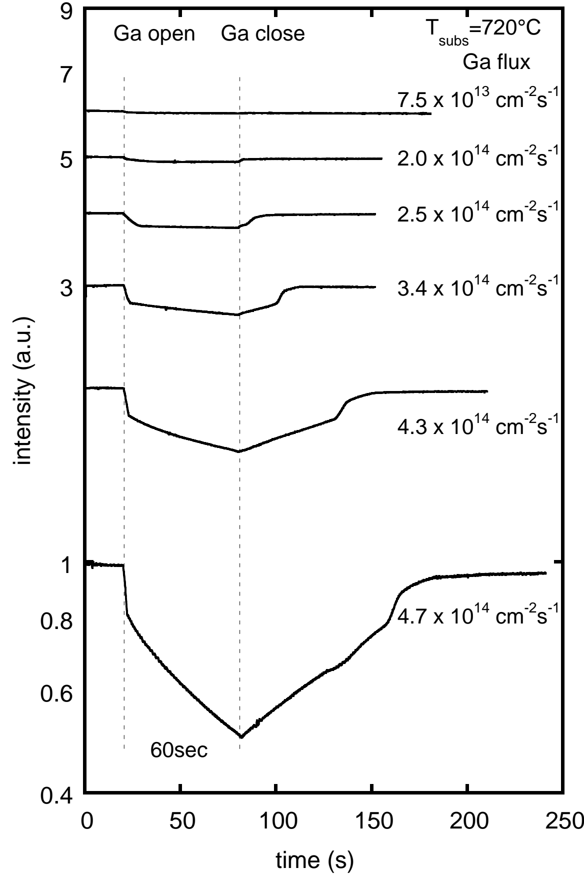

Figure 3.2: The intensity of a reflected high energy electron beam (RHEED intensity) versus time measured during the evaporation of Ga onto c-GaN at a substrate temperature of $T_S = 720°C$. The Ga-fluxes are indicated. The spectra are normalized to one and vertically shifted for clarity.

c-GaN surface was investigated using the intensity of a reflected high energy electron beam (short RHEED intensity) as a probe. The transient of the RHEED intensity of the (0,0) streak was recorded versus time. A sketch of the sample structure and the RHEED geometry is given in Fig. 3.1 a). Figure 3.1 b) shows a RHEED pattern of the (-110) azimuth of a c-GaN surface with a (2×2) reconstruction. The picture was taken during growth interruption. The red window indicates the area of the (0,0) streak where the RHEED intensity was recorded.

The calibration has been performed as follows: All experiments used for the RHEED

intensity observations were started on a Ga-free c-GaN surface established by a 5 min growth interruption. After 5 min the c-GaN surface was exposed to different Ga-fluxes for 60 s. Figure 3.2 shows the variation of the RHEED intensity versus time measured after exposing c-GaN at $T_S = 720°C$ to Ga fluxes between 7.5×10^{13} $cm^{-2}s^{-1}$ and 7.5×10^{14} $cm^{-2}s^{-1}$. For the lowest flux of 7.5×10^{13} $cm^{-2}s^{-1}$ no change in the RHEED intensity was observed indicating the re-evaporation of Ga from the surface. At higher

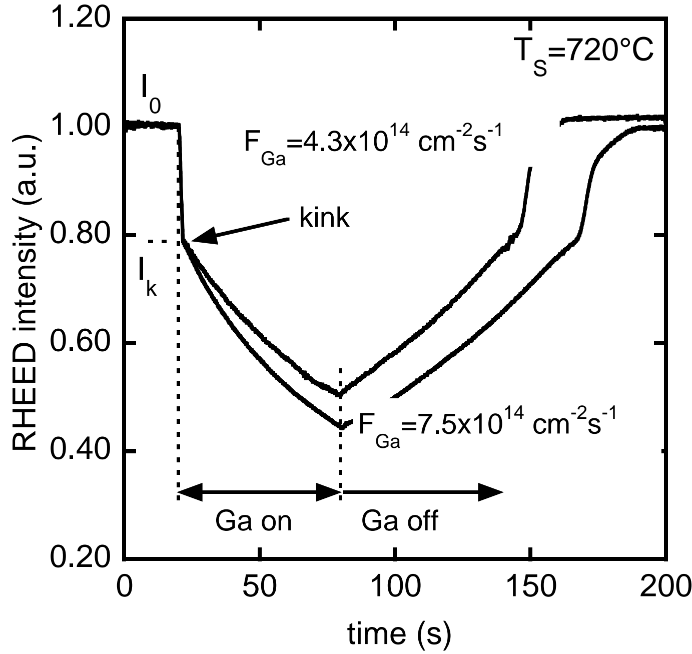

Figure 3.3: RHEED intensity transient for a Ga-flux of $F_{Ga} = 4.3 \times 10^{14}$ $cm^{-2}s^{-1}$ and 7.5×10^{14} $cm^{-2}s^{-1}$.

fluxes $\geq 2.5 \times 10^{14}$ $cm^{-2}s^{-1}$ the RHEED intensity exhibits a clear drop after the Ga shutter was opened. In the following, we discuss the adsorption kinetics in more detail. After opening the Ga shutter we observe a steep decrease of the RHEED intensity between I_0 and a kink position (I_k) which is clearly visible in Fig. 3.3. We would like to point out that the kink position is always at the same relative intensity for Ga-fluxes exceeding 4×10^{14} $cm^{-2}s^{-1}$. The further decrease of the RHEED intensity below I_k has a different gradient. After closing the Ga shutter an increase of the RHEED intensity is observed

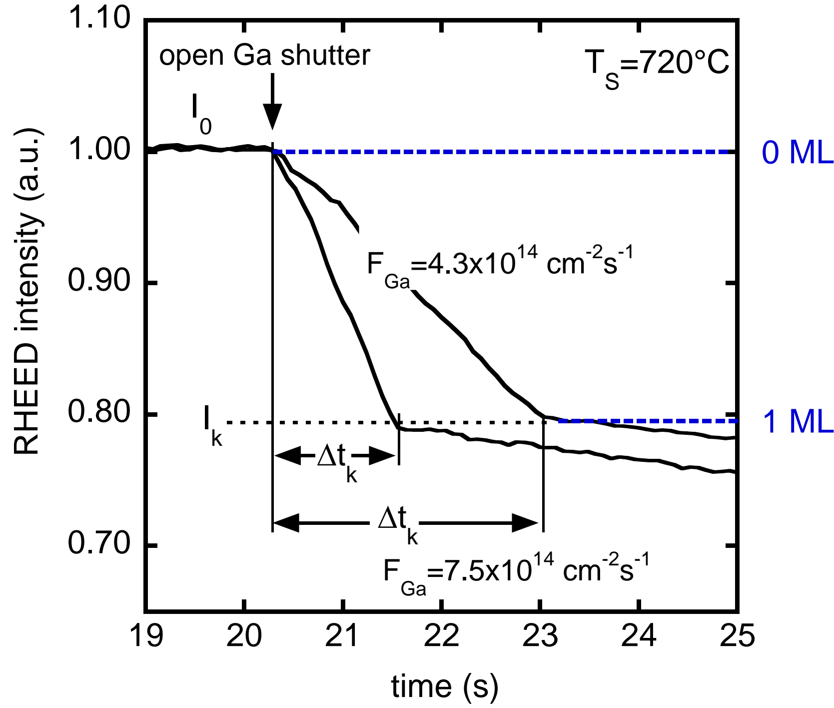

Figure 3.4: RHEED intensity transients for Ga-fluxes of 4.3×10^{14} $cm^{-2}s^{-1}$ and 7.5×10^{14} $cm^{-2}s^{-1}$. After a transition time Δt_k a kink in the transients is observed. The estimated Ga-coverage is plotted on the right side.

which is due to desorption of accumulated Ga. Again two different slopes which change at I_k are observed. The last desorption stage corresponds to the desorption of a fixed amount of Ga and this amount seems to be identical to that adsorbed during the time the intensity reached the kink. Finally the RHEED intensity reaches the starting value I_0 indicating a Ga-free surface. Figure 3.4 shows the RHEED intensity on an extended scale of the two Ga-fluxes shown in Fig. 3.3 just after opening the Ga shutter. A linear decrease of the RHEED intensity during the time interval Δt_k up to the kink position I_k is observed. The gradient of the RHEED intensity drop is related to the impinging Ga-flux and is inverse proportional to the Ga flux.

In order to explain these adsorption kinetics we assume first a certain reflectivity of the GaN surface (I_0) and a lower reflectivity of a Ga-covered surface. A linear decrease

of the RHEED intensity up to the kink position was observed and second we assume an adsorption of a fixed amount of Ga during the time interval Δt_k. This amount seems to be 1 monolayer (ML) based on the flux times Δt_k product which is equal to the number of lattice sites on a GaN surface. Therefore we plotted the estimated Ga-coverage on the right side in Fig. 3.4. The kink position is always at the same relative intensity for Ga fluxes exceeding $4 \times 10^{14}\ cm^{-2}s^{-1}$. To show that our assumptions are correct we had to develop a model which confirms the adsorption of 1 ML Ga at the kink position.

3.1.2 Kinetic model

In the preceding section we have seen a decrease of the RHEED intensity if Ga is supplied. To understand the adsorption kinetics a model is required to account for adsorption and desorption of Ga. Our model is described by the following equation, which takes into account ad- and desorption of Ga.

$$\frac{d\Theta(t)}{dt} = F_{Ga} - F_{des}\Theta(t) \tag{3.1}$$

where $\Theta(t)$ is the coverage of the surface, F_{Ga} is the impinging Ga-flux and F_{des} is the desorption flux which depends on the coverage of the surface. The RHEED intensity itself was assumed to decrease linearly, due to the decreased reflectivity of a metal covered surface.

Fig 3.5 shows one adsorption curve for a Ga-flux of $2 \times 10^{14}\ cm^{-2}s^{-1}$ together with simulations based on equation 3.1. The RHEED intensity drops to a certain value and saturates. As shown in the figure the situation corresponds to a balance between impinging and desorbing flux. A steady-state Ga-coverage is established at the surface which is independent of deposition time. This can be described by eq. 3.1. For these calculations desorption was taken into account. Three different desorption fluxes of $9.8 \times 10^{13}\ cm^{-2}s^{-1}$, $1.6 \times 10^{14}\ cm^{-2}s^{-1}$ and $1.8 \times 10^{14}\ cm^{-2}s^{-1}$ were used for the simulation. The desorption flux F_{des} can be estimated to a value of $1.6 \times 10^{14}\ cm^{-2}s^{-1}$ due to the

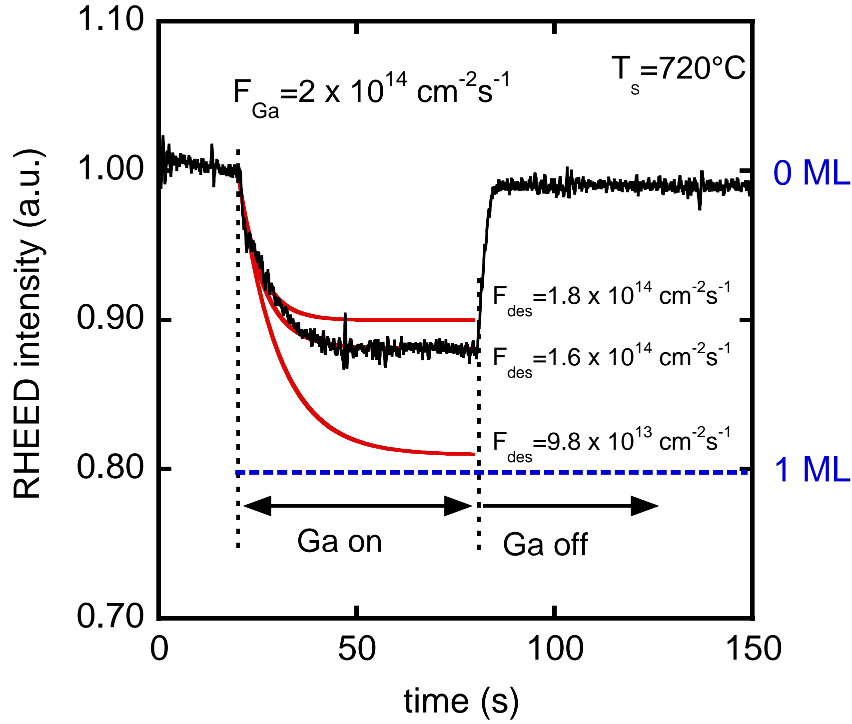

Figure 3.5: RHEED intensity transients for a Ga-flux of $2 \times 10^{14} cm^{-2}s^{-1}$. The red curves show the simulations for a flux of 2×10^{14} $cm^{-2}s^{-1}$ and three different desorption fluxes as indicated in the figure. Good agreement was achieved for a desorption flux of 1.6×10^{14} $cm^{-2}s^{-1}$.

good agreement between experimental and calculated data. On the right side of Fig. 3.5 the estimated values of the Ga-coverage are indicated (see Fig. 3.4). The figure clearly shows that with Ga-fluxes below 4×10^{14} $cm^{-2}s^{-1}$ it is not possible to establish a fully Ga-covered surface.

Corresponding simulations were done for fluxes exceeding 4×10^{14} $cm^{-2}s^{-1}$ taking the desorption flux of 1.6×10^{14} $cm^{-2}s^{-1}$ into account. Figure 3.6 shows the RHEED intensity versus time for two different Ga-fluxes of 4.3×10^{14} $cm^{-2}s^{-1}$ and 7.5×10^{14} $cm^{-2}s^{-1}$ together with simulations based on equation 3.1. The Ga-fluxes are the same as in Fig. 3.4. In Fig. 3.6 the RHEED intensity decreases linearly to the kink position I_k. The simulation also shows a linear decrease during the time interval Δt_k. Based

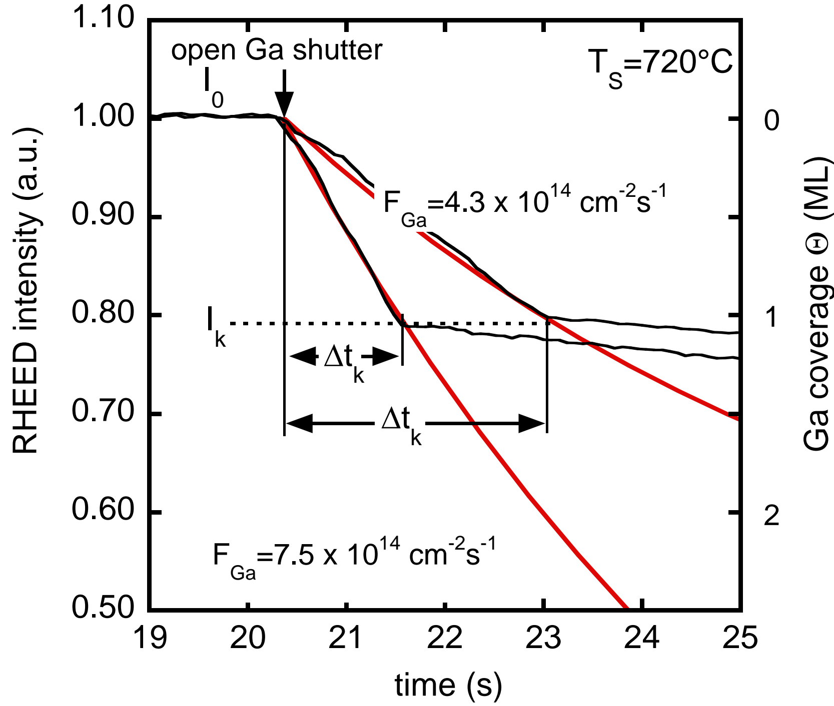

Figure 3.6: RHEED intensity transients for two Ga-fluxes together with simulations as indicated in the figure. Good agreement was achieved within the linear decrease of the RHEED intensity.

on equation 3.1, the simulation reveals a Ga-coverage of 1 ML at the kink position (I_k). The calculated Ga-coverage Θ is indicated on the right side of Fig. 3.6. This confirms our assumption that during Δt_k 1 ML Ga is adsorbed. The further decrease of the RHEED intensity after reaching the kink position is probably related to another adsorption mechanism (Ga-Ga bonds), which change the reflectivity of the electron beam most likely due to increasing interface roughness. This is not considered in our model and therefore the simulated intensity exceeds the kink position.

Using *in situ* reflection high energy electron diffraction, the drop of the RHEED intensity has been calibrated to allow direct measurements of the Ga-coverage. This process established a new method to quantitatively verify the amount of adsorbed Ga on a c-GaN surface between 0 and 1 ML taking I_k as reference.

3.1.3 Growth experiments

In case of c-GaN growth the RHEED intensity transient is different to the experiments described above. An example is plotted in Fig. 3.7 which shows the RHEED intensity measured after opening the Ga shutter.

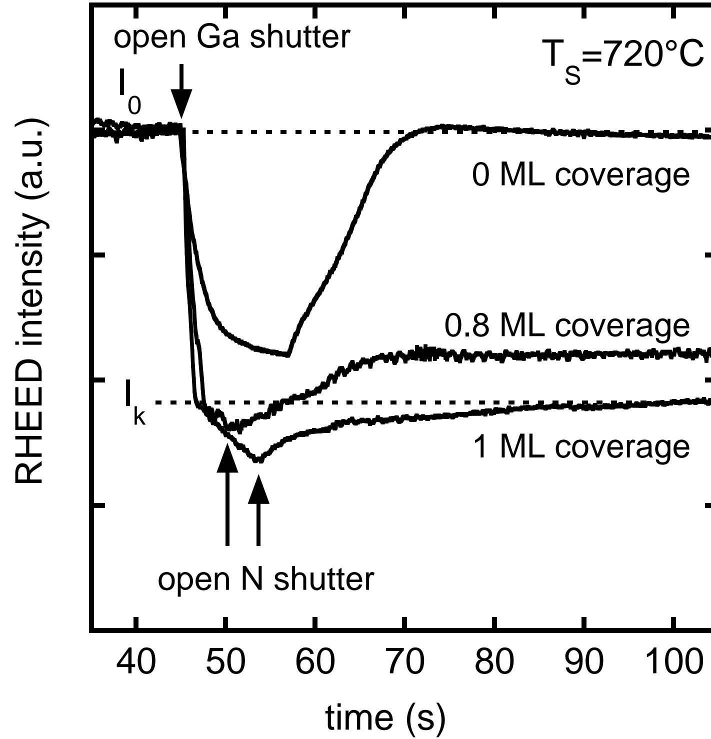

Figure 3.7: RHEED intensity transients measured during the growth of c-GaN, which started after opening the N source. The RHEED intensity measured during growth shows the amount of excess Ga (indicated in the figure) on the c-GaN surface. Ga-fluxes are 4.4×10^{14}, 3.2×10^{14} and 1.2×10^{14} $cm^{-2}s^{-1}$ for the coverages of 1, 0.8, and 0 ML, respectively.

After the RHEED intensity reached the kink position, the N shutter was opened, too (see Fig 3.7. We then observed an increase of the RHEED intensity which is due to the formation of c-GaN. A part of the additional Ga is incorporated into the crystal. During continuing growth the RHEED intensity saturates at a certain value. From the

saturation value the Ga-coverage can be calculated using I_k as reference. This procedure allows measuring the Ga-coverage in the range between 0 and 1 ML with an accuracy of 0.1 ML. We reached a Ga-coverage during c-GaN growth of 0, 0.8 and 1 ML, by varying the Ga-flux. Growth with a coverage of 0 ML is defined as stoichiometric growth, where the incorporation of Ga and N is equal and no adsorbed Ga adlayer exists.
The influence of the Ga-coverage during growth on the surface roughness of c-GaN is depicted in Fig. 3.8. The diagram shows the root-mean-square (RMS) roughness measured on a 5×5 μm^2 AFM scan range of several c-GaN layers versus the Ga-flux used during MBE.

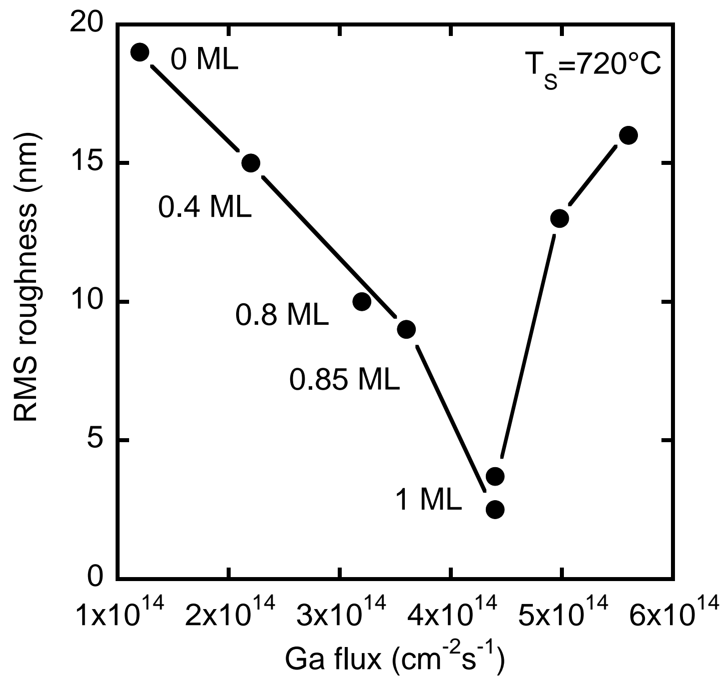

Figure 3.8: Root-mean-square (RMS) roughness of c-GaN layers measured by $5 \times 5 \mu m^2$ scans vs. Ga-flux during growth. The corresponding values of the Ga-coverage during growth are also included. Minimum roughness is obtained with an excess coverage of 1 ML. The line is added for better overview.

The nitrogen flux was almost identical for all samples and the thickness of these samples is about 1 μm. The corresponding values of the Ga-coverage during growth, as

measured by the procedure described above, are indicated in Fig. 3.8. Only values below 1 ML can be measured, because this can be calibrated by the linear decrease of the RHEED intensity up to the kink position. A minimum roughness of 2.5 nm is obtained with 1 ML Ga-coverage during growth. This is in contrast to what has been observed with h-GaN, where optimum growth conditions with regard to surface morphology are related to the formation of Ga bilayer (*c* plane [34], [35] or trilayer (*m* plane [28])).
It has variously been suggested that excess Ga acts as surfactant during epitaxy of hexagonal GaN [34], [36], [37]. We believe that the data shown in Fig. 3.8 clearly demonstrate that this effect exists also on the (001) surface of c-GaN.
The structural properties of these samples were derived from high resolution X-ray diffraction measurements. An $\omega - 2\Theta$ scan of the (002) reflex of sample 1287 is depicted in Fig. 3.9. The reflexes at 41.2 ° and 39.9 ° correspond to the 3C-SiC substrate and the c-GaN layer, respectively.

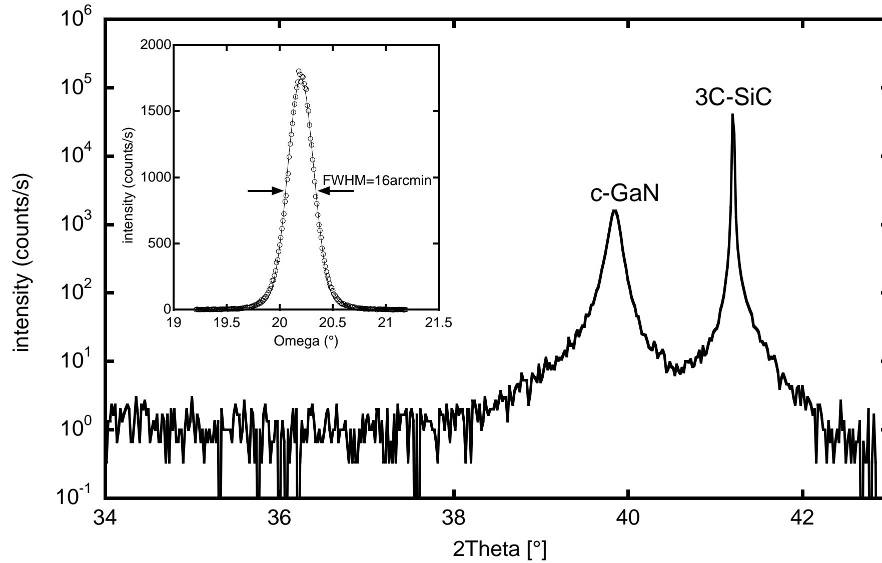

Figure 3.9: $\omega - 2\Theta$ scan of the (002) reflex of sample 1287. The inset shows the ω-scan of this sample revealing a FWHM of 16 arcmin.

No additional peak of the hexagonal (0002) reflex (34.4 °) was detected confirming the absence of h-GaN in growth direction. However, it is well known from c-GaN that

hexagonal inclusions mainly grow on (111) facets and cannot be detected in $\omega - 2\Theta$ scans of the (002) reflex. Therefore reciprocal space maps (RSMs) of the GaN (002) Bragg reflex were measured. The RSMs confirm the absence of hexagonal inclusions on the (111) facets of the cubic layer. Assuming equal X-ray scattering factors of hexagonal and cubic GaN a phase purity $> 99\%$ was estimated from the measurements. In the inset of Fig. 3.9 the rocking curve (ω scan) of sample 1287 is shown. The measured full width at half maximum (FWHM) is about 16 arcmin. The FWHM of ω scans provides information of the dislocation density of the film [32].

The influence of the Ga coverage during growth on the FWHM of the ω scan of c-GaN layers is depicted in Fig. 3.10. The diagram shows the FWHM of the rocking curve of the c-GaN samples shown in Fig. 3.8 versus the Ga-flux used during MBE.

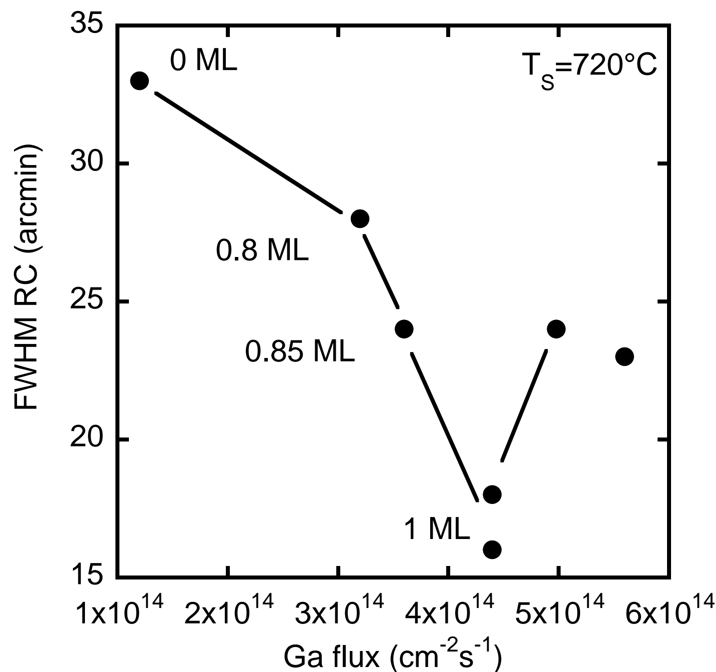

Figure 3.10: Full width at half maximum (FWHM) of c-GaN layers vs. Ga-flux during growth. The corresponding values of the Ga-coverage during growth are also included. Minimum linewidth is obtained with an excess coverage of 1 ML. The line is a guide for the eyes.

The corresponding values of the Ga-coverage during growth, as measured by the procedure described above, are also included in Fig 3.10. The diagram shows a minimum FWHM of the rocking curve for samples grown with a 1 ML Ga-coverage. Among our c-GaN layers with equal thickness, 16 arcmin is a minimum value. Ga-fluxes which are equivalent to a Ga-coverage exceeding 1 ML lead to a pronounced increase of the roughness (see Fig. 3.8) and the full width at half maximum of the X-ray rocking curve.
By comparing the rocking curve linewidth (ω scan) of all our cubic GaN epilayers with the best values cited in literature, the dependence of the FWHM on film thickness has to be taken into account. We found that the linewidth dependence indicates that a defect annihilation process is effective during growth similar to that observed in cubic GaN grown on GaAs (001) substrates [38]. Since in the zinc blende structure the stacking faults (SFs) are on the (111) planes, an annihilation mechanism is possible, when two SFs, for example on the (111) and the (-1-11) planes intersect and annihilate simultaneously with the creation of a sessile dislocation along the [110] direction.

The line width of the rocking curve of the (002) reflex is plotted versus the layer thickness in Fig. 3.11 of cubic GaN epilayers. The red triangles represent our own data, the black dots and the blue squares are data reported by Okumura [39] and Daudin [40]. Both groups used 3C-SiC/Si (001) pseudosubstrates about 3-5 μm thick grown by chemical vapor deposition. As can clearly be seen with improved structural properties of the c-GaN we were able to reach and even exceed under the best cited values. In the case of 3C-SiC, where the lattice mismatch is only -3.7% to cubic GaN, the full green line shows the theoretically calculated FWHM as a function of layer thickness using the dislocation glide model by Ayers [41]. This model implies that the dislocation density N_{disl} is inverse proportional to the layer thickness d and that the FWHM is proportional to $1/d^2$.

The roughness of cubic GaN grown by MBE on freestanding 3C-SiC (001) substrates was significantly reduced by growth under controlled Ga-excess conditions. A minimum RMS roughness of 2.5 nm was achieved using a Ga-coverage of 1 ML during c-GaN growth. Cubic GaN layers grown under these conditions on 3C-SiC substrates have

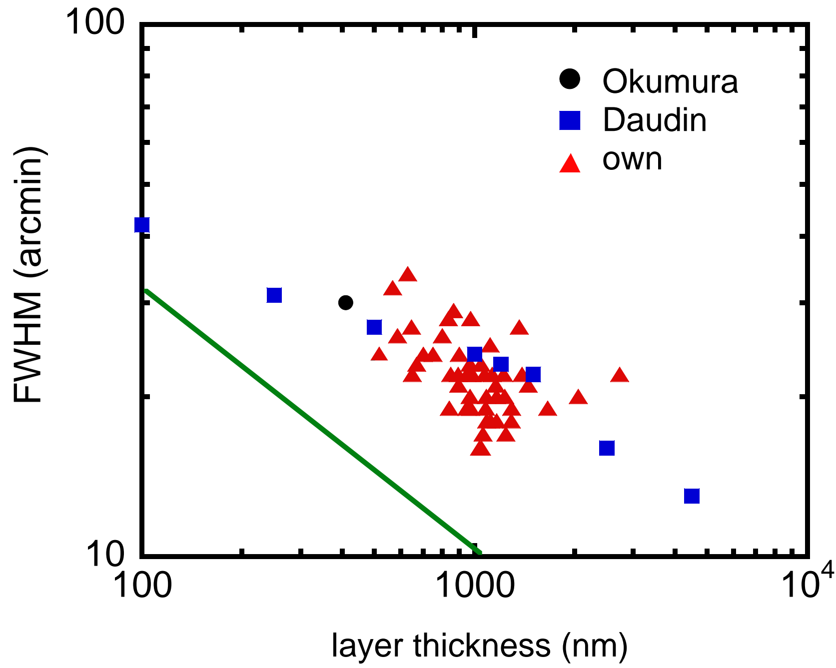

Figure 3.11: Line width of rocking curve (FWHM) of the (002) reflex of cubic GaN epilayers grown on 3C-SiC(001) substrates versus thickness of the GaN epilayers.

narrow X-ray (002) rocking curves (16 arcmin) indicating also a low density of extended defects in these layers. Since the method described above yields the best structural quality of c-GaN epilayers, it was used for the growth process in all further samples.

3.2 Growth and characterization of cubic AlGaN/GaN heterostructures

After optimizing the c-GaN buffer layer, we focus on growth and structural properties of cubic AlGaN. AlGaN is used as barrier layer in AlGaN/GaN quantum well structures and high electron mobility transistors (HEMTs). For the realization of distributed AlGaN/GaN bragg reflectors (DBR) high quality AlGaN is required. For the fabrication of optoelectronic or electronic devices it is essential to realize $Al_xGa_{1-x}N$ epilayers with a well-defined Al mole fraction x which determines e.g. the barrier height of heterojunctions and quantum wells. Therefore a series of heterostructures was grown to check strain, dislocation density, mole fraction and roughness of these heterostructures. The structural parameters were determined by HRXRD and AFM.
A sketch of the grown AlGaN/GaN heterostructures is depicted in Fig. 3.12. On top of a c-GaN buffer an $Al_xGa_{1-x}N$ layer with a thickness between 50 and 400 nm was deposited. The mole fraction of the AlGaN film was varied between x=0.15 and x=0.74.

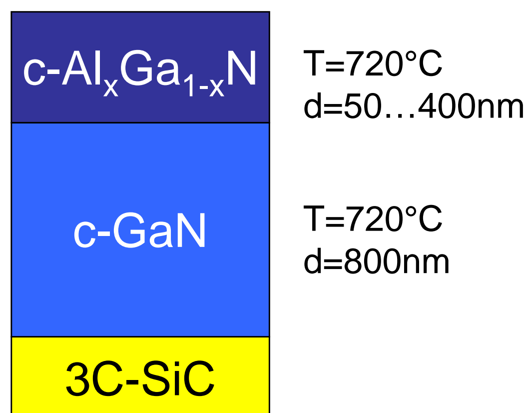

Figure 3.12: Schematic sketch of an AlGaN/GaN heterostructure

The influence of the Ga-coverage on the AlGaN surface during growth was also investigated.
Firstly we will focus on the adjustment of the metal fluxes needed for the growth of c-

AlGaN. As known from the growth of c-GaN, optimum growth conditions were achieved with a well defined Ga-coverage of 1 ML during growth. This knowledge will be transferred to the growth of AlGaN. We will start with the total impinging Ga-flux for c-GaN which is given by

$$F^{imp}_{Ga,1ML}(GaN) = F^{imp}_{Ga,0ML}(GaN) + F^{1Ml,cover}_{Ga} = \frac{F^{inc}_{Ga}(GaN)}{s_{Ga}} + F^{1ML,cover}_{Ga}(GaN) \quad (3.2)$$

where $F^{imp}_{Ga,1ML}$ is the impinging Ga-flux for c-GaN growth with 1 ML coverage as described above, $F^{imp}_{Ga,0ML}$ is the corresponding Ga-flux for stoichiometric growth (see Fig. 3.7), $F^{1ML,cover}_{Ga}$ is the Ga-flux necessary for the formation of an additional Ga-coverage of 1 ML during growth. F^{inc}_{Ga} is the incorporated Ga-flux and s_{Ga} is the sticking coefficient of Ga. The Ga sticking coefficient strongly depends on the growth temperature and the value is about 0.5 for a growth temperature of 720°C. Details are discussed in Ref. [42]. We get the impinging Ga-flux $F^{imp}_{Ga,0ML}$ for stoichiometric growth conditions from Fig. 3.7. This metal flux ($F^{imp}_{Ga,0ML} \cdot s_{Ga} = F^{inc}_{Ga}$) has to be used to calculate the Al and Ga-fluxes for $Al_xGa_{1-x}N$ growth. Therefore we have to split F^{inc}_{Ga} into the following eq.

$$F^{imp}_{Al}(AlGaN) = \frac{x \cdot F^{inc}_{Ga}(GaN)}{s_{Al}} \quad (3.3)$$

and

$$F^{imp}_{Ga}(AlGaN) = \frac{1 - x \cdot F^{inc}_{Ga}(GaN)}{s_{Ga}} \quad (3.4)$$

where x is the Al mole fraction, s_{Al} the sticking coefficient of Al (1 for $T_S = 720°C$) and $F^{imp}_{Ga,Al}(AlGaN)$ are the Al and Ga-fluxes needed for AlGaN growth. These fluxes are for stoichiometric AlGaN growth. For c-AlGaN we have to add the Ga-flux which is necessary to establish a 1 ML Ga-coverage during growth, thus eq. 3.4 has to be modified to

$$F^{imp}_{Ga}(AlGaN) = \frac{1 - x \cdot F^{inc}_{Ga}(GaN)}{s_{Ga}} + F^{1ML,cover}_{Ga} \quad (3.5)$$

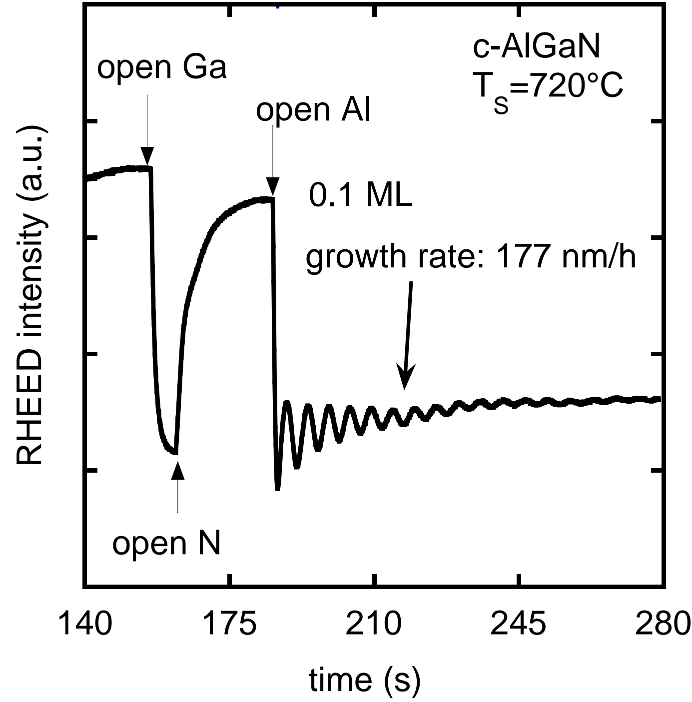

Figure 3.13: RHEED intensity measured during initial growth of $c-Al_{0.25}Ga_{0.75}N$. The RHEED intensity after opening the N shutter yields the amount of excess Ga on the c-GaN surface. After opening the Al shutter RHEED intensity oscillations are observed indicating a two-dimensional growth mode with a rate of 177 nm/h.

Figure 3.13 shows the RHEED intensity during initial growth of a c-AlGaN layer using the fluxes described above (eqs. 3.3 and 3.5). When the nitrogen shutter was opened with Ga on, an increase of the RHEED intensity was observed, indicating a Ga-coverage of about 0.1 ML (see Fig. 3.13. This is due to the reduced Ga-flux in comparison to pure c-GaN growth. Then the Al shutter was opened and the RHEED intensity dropped revealing a surface coverage of about 1 ML. The increase of the coverage is given by the additional metal flux and contains an exchange process in which the Ga incorporation in the layer is depleted by the Al. This process is driven by the higher bond energy of Al-N which is about $E_{AlN} = 2.88eV$ [43] in comparison to Ga-N bond energy of $E_{GaN} = 2.24eV$ [43]. Weakly damped RHEED oscillations were observed, indicating

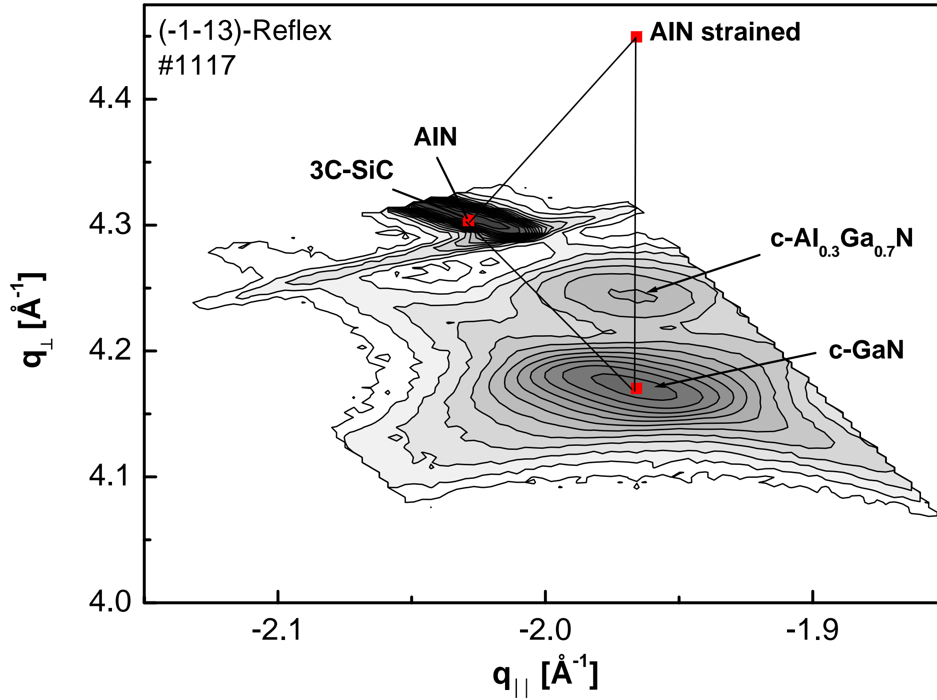

Figure 3.14: Reciprocal space map of the c-GaN (-1-13) reflex of sample 1117. The c-AlGaN layer is pseudomorph to the c-GaN buffer layer. The Al-mole fraction is x=0.3

a two-dimensional AlGaN growth at a substrate temperature of $T_S = 720°C$ with a growth rate of 177 nm/h. These are the first RHEED oscillations observed in cubic AlGaN epitaxy.

For the growth of quantum wells it is essential to achieve the correct alloy composition. Therefore XRD reciprocal space maps (RSMs) of the c-GaN (-1-13) reflex of different AlGaN layers were measured to check the composition. Within these RSMs it is also possible to measure the strain of the heterostructures. Strain is another parameter which influences the dislocation density. With increasing relaxation of the lattice the defect density increases. Figure 3.14 shows a RSM of the c-GaN (-1-13) reflex of sample 1117. The thickness of the c-AlGaN layer is about 100 nm. The reflexes plotted in the figure correspond to the 3C-SiC substrate, the c-GaN buffer and the c-AlGaN layer. In addition, the position of the Bragg reflexes of c-GaN, strained c-AlN and relaxed c-AlN

are indicated. They were calculated with the lattice parameters of 4.38 Å for c-AlN. The parameters of c-GaN and c-AlN are given in the appendix. The position of the c-AlGaN reflex relative to the c-GaN reflex indicates that the c-AlGaN layer is pseudomorph to the c-GaN buffer layer. The Al mole fraction of this layer is x=0.3.

The strain strongly depends on the thickness and the composition of the AlGaN layer. Details are described in Ref. [44], [45]. With increasing thickness the strain energy increases and with increasing Al mole fraction the critical thickness (see Ref. [45], [46]) decreases.

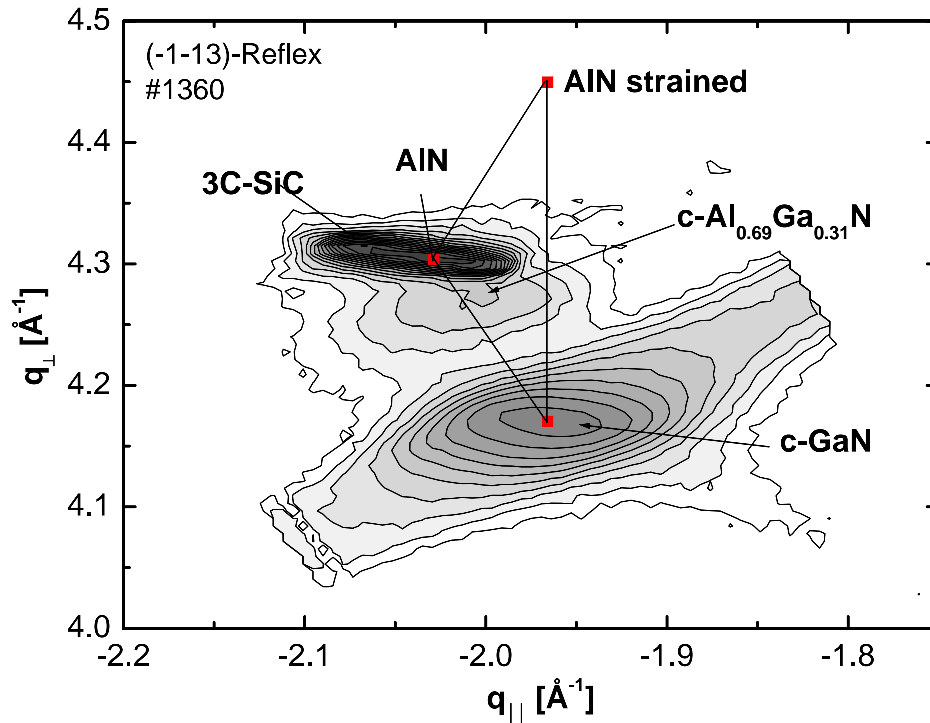

Figure 3.15: Reciprocal space map of the c-GaN (-1-13) reflex of sample 1360. The c-AlGaN layer is relaxed to the c-GaN buffer layer. The Al-mole fraction is x=0.7

An example for a relaxed AlGaN layer is shown in Fig. 3.15. The RSM of the c-GaN (-1-13) reflex is plotted. The thickness of the AlGaN layer is 80 nm and the layer is nearly relaxed. The Al mole fraction of this layer is x=0.69. With increasing mole

fraction of the $Al_xGa_{1-x}N$ layer the defect density also increases due to the increasing lattice mismatch between the c-GaN buffer and the c-$Al_xGa_{1-x}N$ layer.

Figure 3.16 shows the XRD ω scans of the c-GaN buffer and the c-AlGaN layer of sample 1117. The c-$Al_{0.3}Ga_{0.7}N$ layer is pseudomorph to the c-GaN buffer which means that no more dislocations are created at the heterointerface (see Fig. 3.14). This was confirmed by measuring the XRD ω scan of both layers.

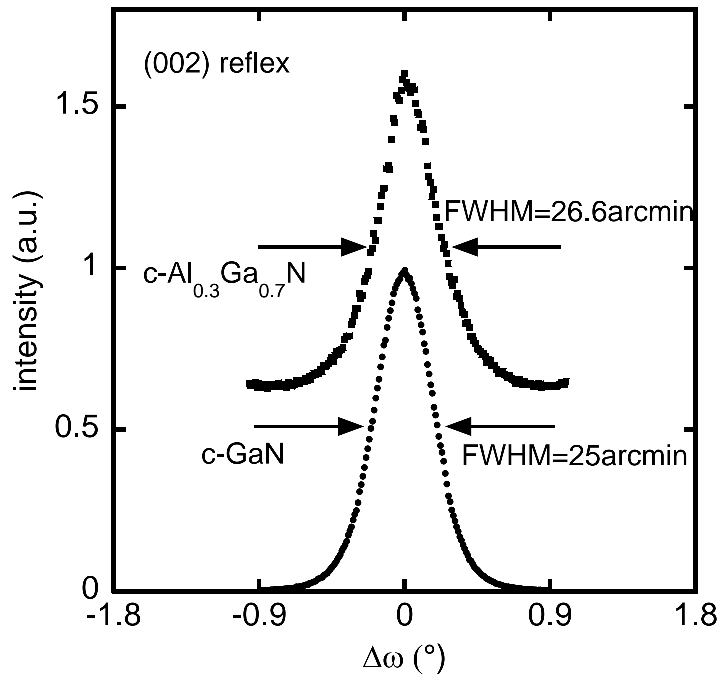

Figure 3.16: XRD rocking curve of the (002) reflex of sample 1117. The full width at half maximum of the c-GaN and the c-AlGaN layer are nearly identical.

The measured values of the FWHM are 25 arcmin for the c-GaN buffer and 26.6 arcmin for the c-AlGaN layer. These values are nearly identical indicating the same dislocation density in both layers. For relaxed AlGaN the FWHM of the XRD rocking curve is about two times higher than in strained layers.

A series of samples was grown using a Ga-coverage of 1 ML at a substrate temperature of 720°C. The relation of the Al mole fraction to the flux ratio of the Al-flux to the total metal flux is depicted in Fig. 3.17.

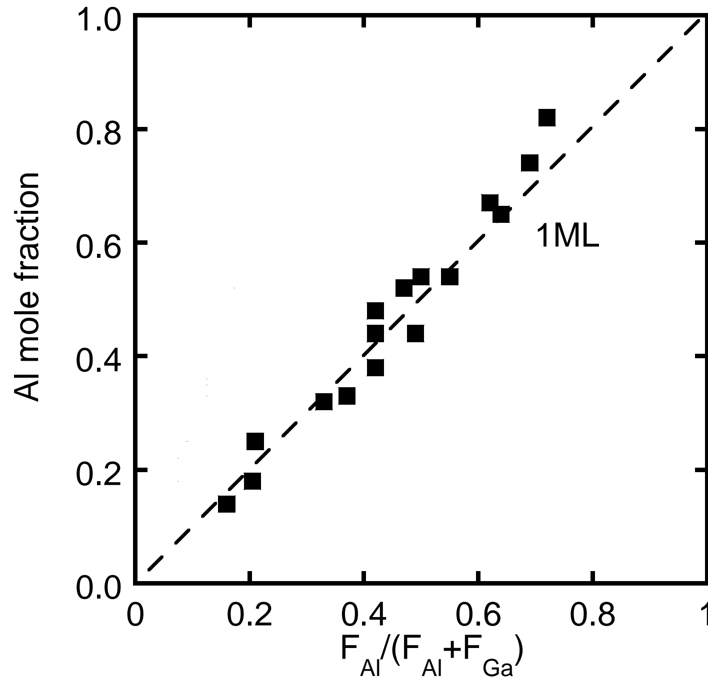

Figure 3.17: Relation between the Al mole fraction x of c- $Al_xGa_{1-x}N$ and the ratio of Al-flux to the total metal flux for films grown under 1ML Ga-coverage. The mole fraction x was determined by HRXRD.

We found that the Al mole fraction x is directly proportional to the Al mole fraction in the vapor phase for the samples grown with a 1 ML Ga-coverage, indicating that Al is preferentially incorporated.
The RMS roughness of different $Al_xGa_{1-x}N$ alloys versus the Al mole fraction is plotted in Fig. 3.18. The diagram shows that the RMS roughness measured on a 5×5 μm^2 scan is constant with a value of about 5 nm for $Al_xGa_{1-x}N$ in the range of x=40% to x=70%. However, these values are slightly above the minimum value of c-GaN which may be due to the lower surface diffusion of Al in comparison to Ga, because AlGaN is normally grown at higher substrate temperatures. The RMS value for pure AlN is about 1 nm. Similar observation were also made with GaAs and AlAs where the ternary compound shows a higher roughness than the two binary layers. The roughness of AlGaN layers exceeding 1 ML coverage are about a factor of two higher [44], [45].

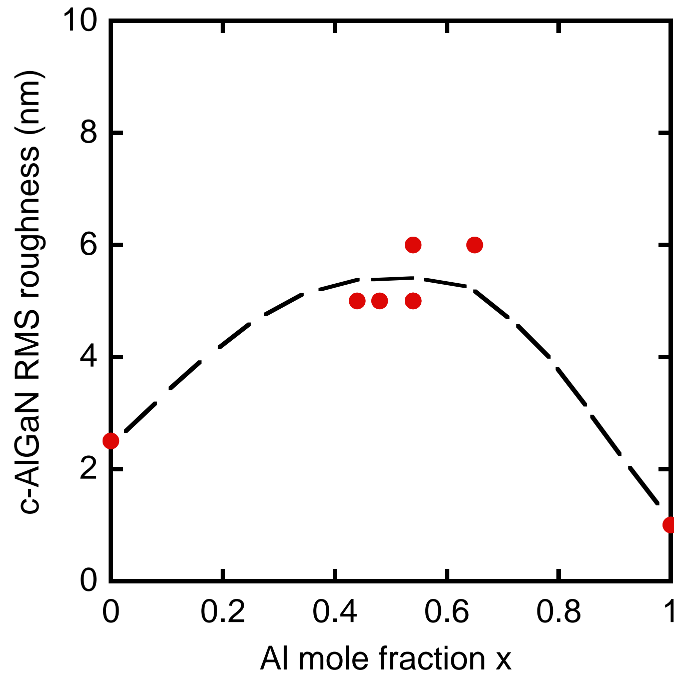

Figure 3.18: RMS surface roughness of different c-$Al_xGa_{1-x}N$/GaN heterostructures with an Al mole fraction between x=0 and x=1. Layers were grown with a 1 ML Ga coverage. The line is a guide for the eyes.

Based on the results described in this chapter, we assume that AlGaN layers up to a thickness of 80 nm and a Al mole fraction up to x=0.5 are pseudomorph to the c-GaN buffer layer. The dislocation density is equal to that of the buffer layer. AlGaN layers of that thickness can be used for the growth of AlGaN/GaN-based quantum structures where the thickness of the AlGaN layer is less than 100 nm. The growth and the properties of AlGaN/GaN quantum wells will be discussed in the next chapter.

4 Growth of cubic AlGaN/GaN quantum wells

This chapter deals with AlGaN/GaN single (SQW) and multiple quantum wells (MQW) grown on c-GaN buffer layers. Firstly the growth and the structural properties of these quantum wells are discussed. Then the optical properties of these structures are investigated. The optical properties of nonpolar cubic quantum wells are compared to their hexagonal counterparts grown along different growth directions. We found that c-AlGaN/GaN QWs are unaffected by internal piezoelectric and polarization fields.

4.1 Growth and structural properties of cubic AlGaN/GaN quantum wells

Two types of c-AlGaN/GaN quantum wells, i.e. single and multiple quantum wells (SQWs and MQWs) were grown. Figure 4.1 shows a schematic sketch of a multiple quantum well structure.

Before the quantum structure was grown a 800 nm thick c-GaN buffer layer was deposited on the 3C-SiC substrate. The buffer and the c-AlGaN/GaN quantum wells were grown at a substrate temperature of 720°C. The layers were deposited using a 1 ML coverage as described in the previous chapter [31]. The MQWs consist of 6 nm thick $Al_xGa_{1-x}N$ barriers and GaN wells with a thickness of 2.5 to 7.5 nm, and were sandwiched between 50 nm AlGaN cladding layers. The metal fluxes were adjusted using

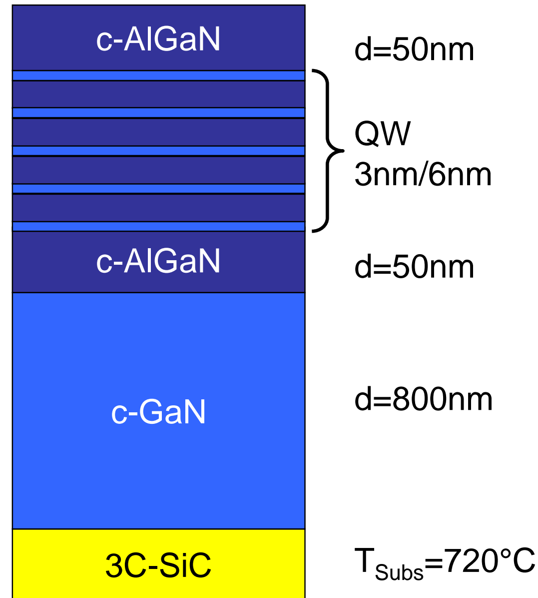

Figure 4.1: Schematic Sketch of a multiple quantum well structure

equations 3.3 and 3.4 given in chapter 3. During change between GaN well and AlGaN barrier the growth was stopped for 5 min to change the temperature of the Ga source to adjust the correct flux. The surface was continuously monitored during growth by RHEED. At the initial growth of the c-AlGaN layers weakly damped oscillations of the intensity of the RHEED specular spot were observed.
The structural characterization was performed by HRXRD. We measured $\omega - 2\Theta$ scans of the symmetric (002) reflex and reciprocal space maps of the (-1-13) reflex of the c-$Al_xGa_{1-x}N$ quantum structures. Figure 4.2 shows an $\omega - 2\Theta$ scan of the (002) reflex of sample 1372. This sample consists of a 15 period $Al_xGa_{1-x}N$/GaN MQW structure.

The reflexes of the 3C-SiC substrate and of the c-GaN buffer as well as several superlattice peaks are clearly resolved. The broadening of the peaks is mostly dominated by the interface roughness, which is in the order of 2-3 nm. Experimental data have been fitted using the dynamic scattering theory [47], yielding a well width of 3 nm, a barrier width of 6 nm and an Al mole fraction of x=0.3. The values of the thickness are

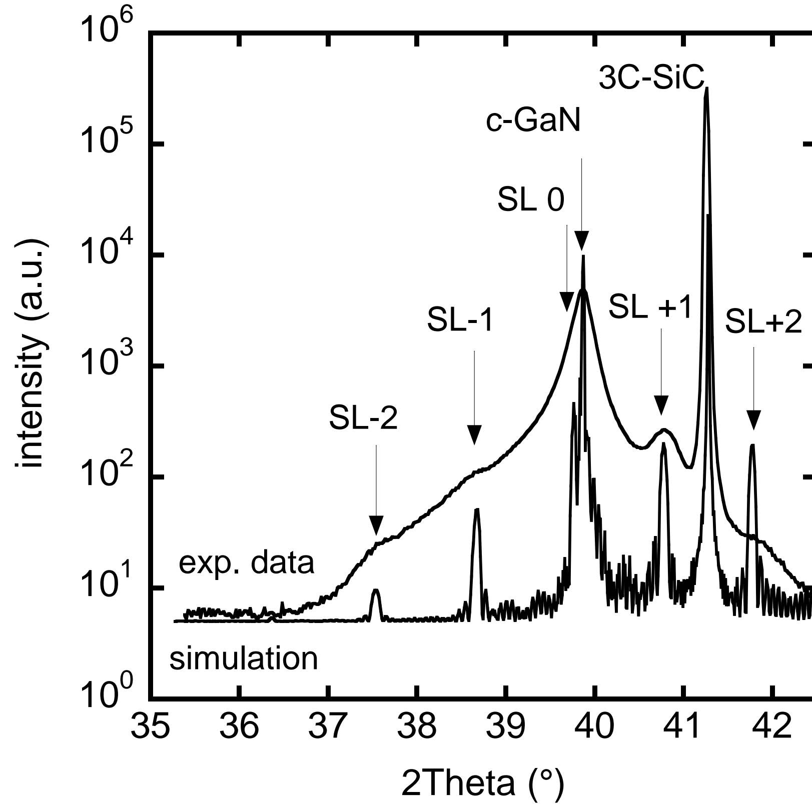

Figure 4.2: Measured $\omega - 2\Theta$ scan of a 15-fold $Al_{0.3}Ga_{0.7}N$/GaN structure (solid line) and simulated data (dotted line). The well and the barrier width are 3 nm and 6 nm.

in excellent agreement with the data, obtained from growth rate measurements using RHEED oscillation period. The full width at half maximum (FWHMs) of XRD rocking curves of the c-GaN buffer and the AlGaN cladding layers were almost identical, revealing that the density of dislocations does not increase at the AlGaN/GaN interface. The reciprocal space map around the asymmetric (-1-13) reflex depicted in Fig. 4.3 shows that the quantum structure is pseudomorph to c-GaN buffer. Clear superlattice peaks of the c-AlGaN/GaN quantum structure are observed and indicated in the figure. The peaks of the c-GaN buffer and the 3C-SiC substrate are also indicated.

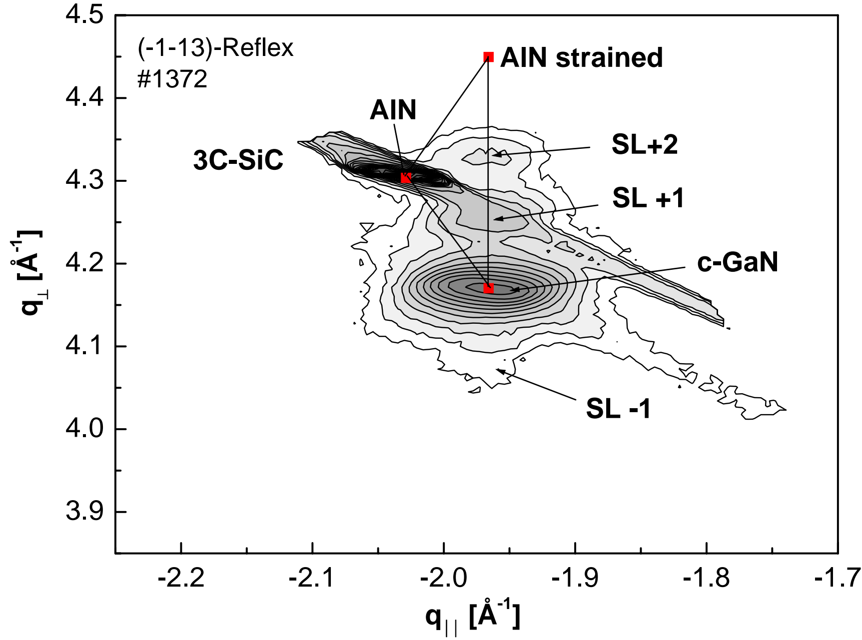

Figure 4.3: Reciprocal space map around the asymmetric (-1-13) reflex of sample 1372. The quantum wells are pseudomorph to the c-GaN buffer.

4.2 Photoluminescence of cubic AlGaN/GaN quantum wells

The optical transition energies of our QW structures were derived by room and low (2 K) temperature photoluminescence spectroscopy using the 325 nm line of a HeCd laser. Figure 4.4 shows the room temperature PL spectra of a single quantum well (SQW) structure (left) and a 5 period multiple quantum well (MQW) structure (right). The quantum structure has 3 nm thick wells and 6 nm thick barriers and is sandwiched between two 50 nm thick cladding layers. The Al mole fraction of the AlGaN barriers is x=0.15 [48]. Strong emission at 3.28 eV for the SQW and at 3.30 for the MQW is observed. The emission lies between the c-GaN emission at 3.20 eV and the emission of the $Al_{0.15}Ga_{0.85}N$ cladding layer at about 3.48 eV [23]. Therefore we related the observed strong ultraviolet emission to radiative recombination of electron-hole pairs in the QWs.

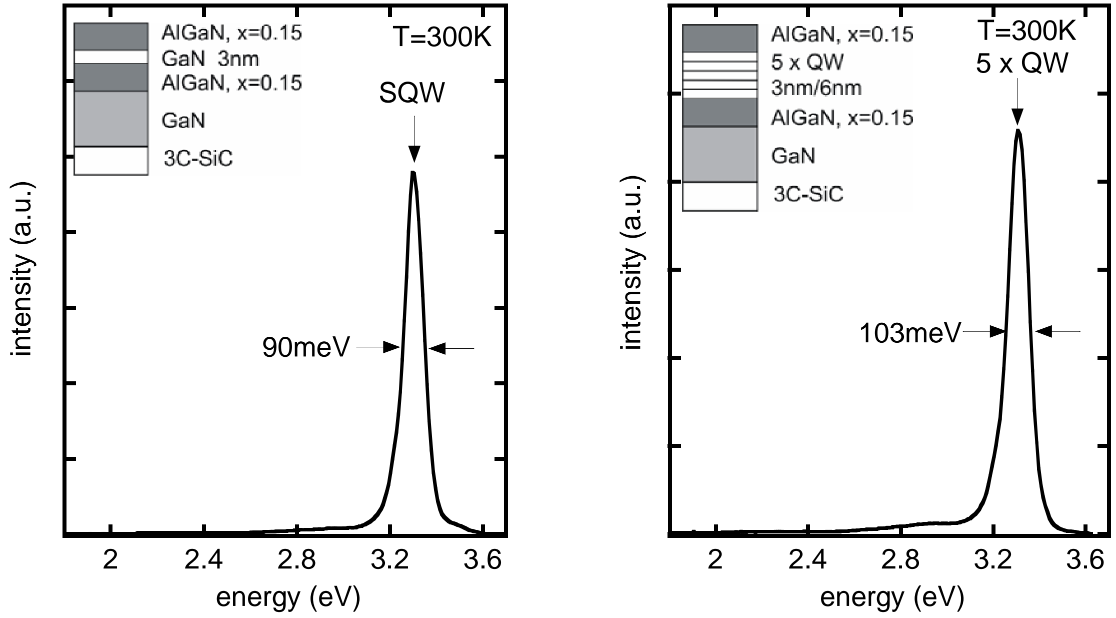

Figure 4.4: Room temperature photoluminescence of cubic $Al_{0.15}Ga_{0.85}N$/GaN single and multiple quantum well structures. The QW transition energy is E=3.30 eV and the linewidth is 90 meV for the SQW and 103 meV for the MQW.

The emission of the AlGaN barriers is suppressed due to an efficient collection of excess carriers from the barriers in the well region indicating a diffusion length of about 50 nm in the AlGaN barriers, which is in good agreement with earlier results of cathodoluminescence investigations [49]. No additional yellow luminescence at about 2.25 eV which is related to defects in nitrides was observed [4]. The linewidths of the room temperature QW emission are 90 meV for the SQW and 103 meV for the MQW. The low temperature (2 K) Pl spectra of the SWQ and MQW structures are shown in Fig. 4.5. The emission of the SQW lies at 3.33 eV and at 3.35 for the MQW. The linewidth is 64 meV for the SQW and 80 meV for the MQW. The additional peaks indicated as (D^0A^0) and (X) originate from the donor-acceptor pair transition and the free exciton transition of the underlying cubic GaN layer. This is most likely due to the penetration depth (about 400 nm) of our HeCd laser, which excites electron-hole pairs in the underlying c-GaN

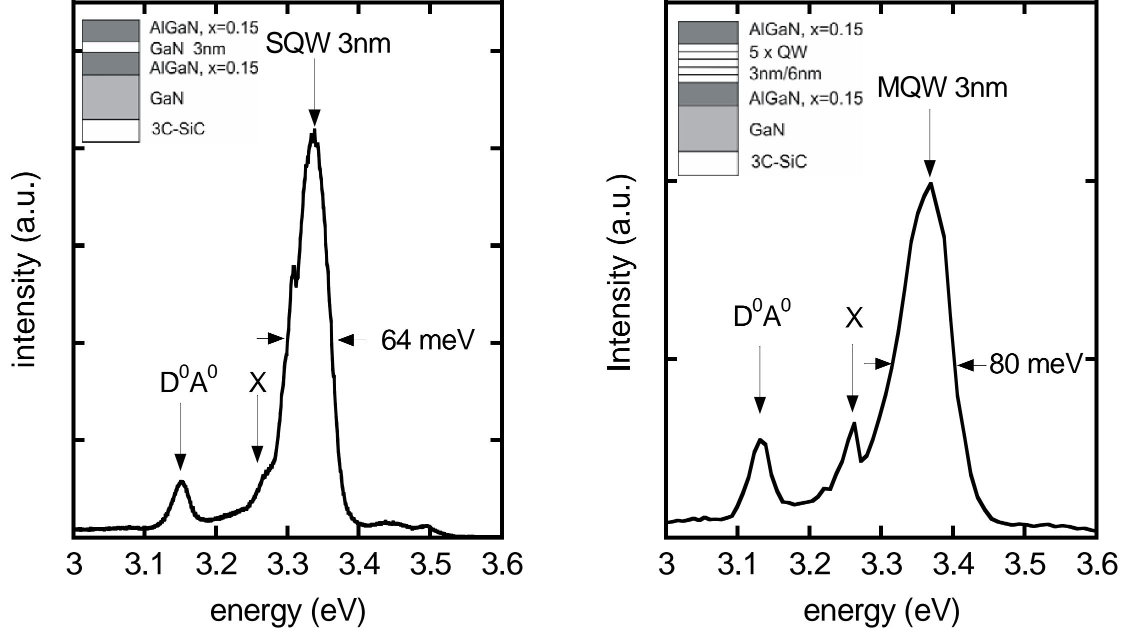

Figure 4.5: Low temperature photoluminescence of cubic $Al_{0.15}Ga_{0.85}N$/GaN SQW and MQW structures. The QW transition energy is E=3.33 eV and 3.35 eV and the linewidth is 64 meV and 80 meV, respectively

layer. The difference in the peak energies is due to the temperature shift between room and low temperature [50]. We suppose that the difference of the SQW and the MQW linewidths at room temperature and at low temperature is due to fluctuations of the width of individual quantum wells in the MQW structure. Notably, the linewidth of the c-$Al_{0.15}Ga_{0.85}N$/GaN QW emission is close to values recently reported for hexagonal AlGaN/GaN quantum wells grown on *a*-plane substrates [4] [51]. This indicates the potential of cubic quantum structures for application in nonpolar devices. However, the PL linewidth of our QWs exceeds that of the emission from polar (*c*-plane) hexagonal AlGaN/GaN QWs [52], this is most likely due to the higher density of dislocations in metastable cubic structures.

The presence of internal piezoelectric fields in hexagonal nitride based quantum structures give rise to a strong quantum confinement Stark effect (QCSE) leading to a red-shift

of the quantum well emission. The energy band diagram of a cubic quantum well and of a state-of-the-art hexagonal quantum well grown along the polar c-axis is plotted in Fig. 4.6. In the case of cubic nitrides the electron and hole wave functions are localized in

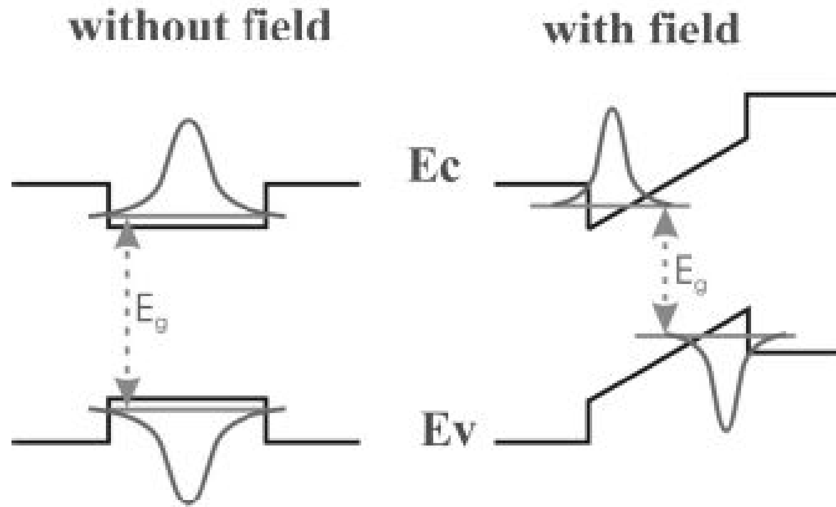

Figure 4.6: Schematic view of a quantum well without and with built-in field. Electrons and holes are localized in opposite corners leading to a red-shift of the lowest transition and to a reduction of the oscillator strength compared to the flat band case in the cubic system [53].

the center of the quantum well whereas for the hexagonal counterpart the electron and hole wave functions are separated and localized opposite side of the quantum well edges. Due to the spatial separation of electrons and holes the oscillator strength is strongly reduced and as a result the recombination probability of electron and hole pairs will be severely lowered [3] resulting in a weak luminescence intensity.
The room temperature PL peak energies of our cubic $Al_{0.15}Ga_{0.85}N/GaN$ MQWs are plotted versus well width in Fig. 4.7 together with hexagonal $Al_{0.17}Ga_{0.83}N/GaN$ quantum wells [54]. The figure shows the energy difference ΔE of the transition energies of the quantum wells to the bulk GaN versus the quantum well thickness. We find a decrease of the transition energy with increasing well width.

The full curve in Fig. 4.7 is calculated using a square well self-consistent Poisson-

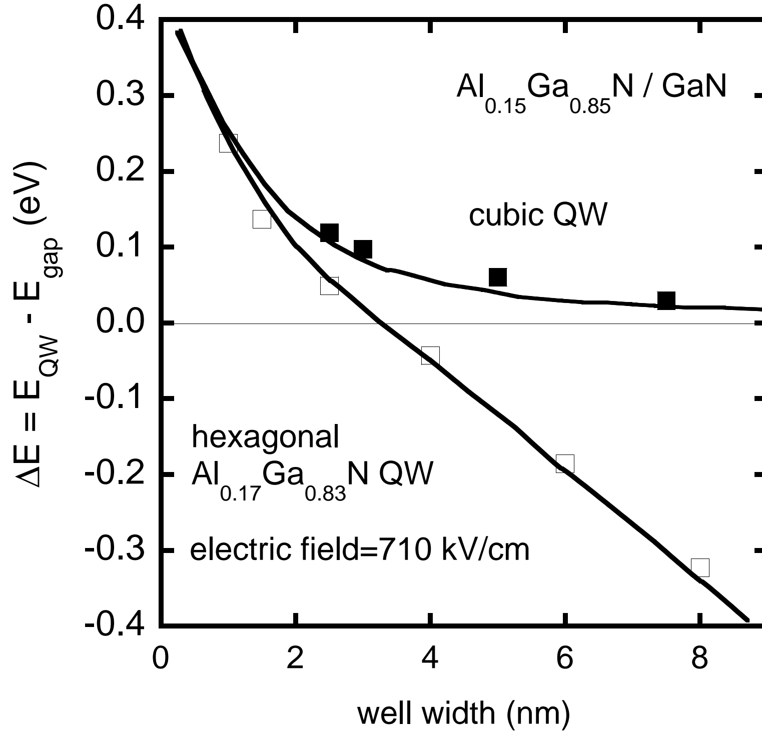

Figure 4.7: Energy difference of cubic and hexagonal AlGaN/GaN QWs as a function of well width [54]. The full curve for the cubic QWs was calculated using the self-consistent Poisson-Schrödinger model [55]. The hexagonal QWs show a red-shift of the transition energy below the band gap of hexagonal GaN.

Schrödinger calculation of the quantum well [55]. We assume a 70:30 ratio of the conduction and the valence band discontinuities [56]. The effective masses of electrons and holes in c-GaN and c-$Al_{0.15}Ga_{0.85}N$ are $m_e = 0.15m_0$ [57], $m_h = 0.8m_0$ and $m_e = 0.156$, and $m_h = 0.86$ [58], respectively. We find excellent agreement between experimental and calculated data indicating that, unlike in polar h-group III-nitride based quantum structures, polarization and piezoelectrical fields are absent in c-III-nitrides with a (001) growth direction [59]. The shift of the emission energy versus the width of cubic QWs is almost identical to that of nonpolar a-plane hexagonal AlGaN/GaN QWs with similar composition [51]. The transition energies E_{QW} in the hexagonal case are lower than the band gap of hexagonal GaN due to the quantum confinement Stark effect. The strength

of the electric fields in hexagonal GaN increases with increasing Al content and is about 710 kV/cm for an Al mole fraction of x=0.17 [54].

5 AlN/GaN superlattices for intersubband spectroscopy

AlN/GaN superlattices were grown on c-GaN buffer layers. These structures are used for intersubband spectroscopy in the infrared (IR) region and can be used as detector for this kind of radiation. A brief introduction on intersubband spectroscopy is given below. The main part of this chapter will focus on the growth of AlN/GaN superlattices followed by optical investigation of these structures. The optical transition energies were calculated and compared to experimental results. First intersubband transitions were observed in cubic III-nitrides.

5.1 Intersubband transitions

While most of the applications of III-nitride materials are in the visible and the ultra-violet spectral region, there has been increasing interest in this class of materials for the infrared spectral range. This interest stems from the fact that AlN/GaN systems exhibits a large conduction band offset that allows to optically design structures with intersubband transitions. Additionally, the intersubband transition relaxation time in GaN/AlGaN was predicted theoretically [60] [61] to be 100 fs at 1.55 μm, which is one order of magnitude shorter than the relaxation time in InGaAs multiple quantum wells. Intersubband transitions in AlN/GaN multiple quantum wells have been investigated for their application possibilities in the near infrared spectral region by several groups [62],

[63], [64], [65], [66], [67], [68], [69].

$Al_xGa_{1-x}N$/GaN or AlN/GaN multi quantum wells are suitable for detection of near infrared light. To make this possible the size of the wells must approach the size of the exciton Bohr radius of the well material. The effective Bohr radius in GaN is about 28 Å due to the large effective mass. The small size of the Bohr radius in GaN materials necessitates the use of small well sizes to achieve quantization of energy levels. One difference between quantum well infrared photodetectors (QWIP) and other IR detectors is that optical absorption takes place within sub-bands in the conduction or valence band. Transitions in the wells due to photon absorption are commonly called intersubband

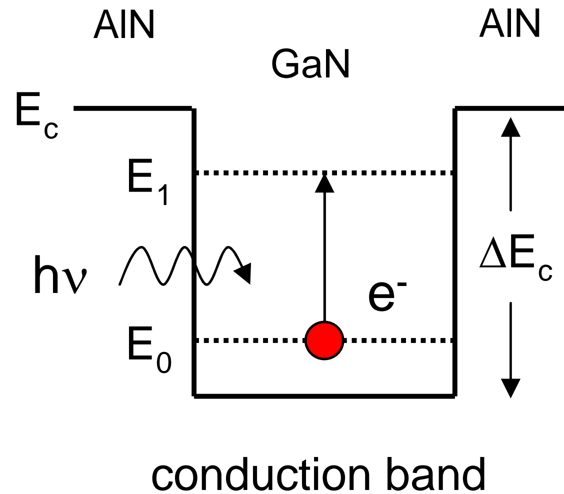

Figure 5.1: Schematic sketch of an intersubband transition in the conduction band after absorption of a photon with equal energy to the difference between the ground state E_0 and the first excited state E_1 [70].

(or intraband) transitions. These transitions take place in the conduction band if the semiconductor is n-type doped or in the valance band if the semiconductor is p-type doped. Due to the fact that we used only n-type GaN we will focus on the conduction band to illustrate the intersubband transition. Figure 5.1 shows a schematic sketch of an intersubband transition in the conduction band. The quantized states are E_0 and E_1

as indicated. The ground state is populated by electrons due to n-type doping which means that the Fermi energy has to be above the ground state energy. If an electron in the ground state E_0 absorbes a photon it can induce a transition to the first excited state E_1 if the photon energy is equal to the energy difference between E_0 and E_1. This transition is called bound-to-bound transition. However, this is not always the case. Two other types of intersubband transitions have to be considered (see Fig. 5.2). The

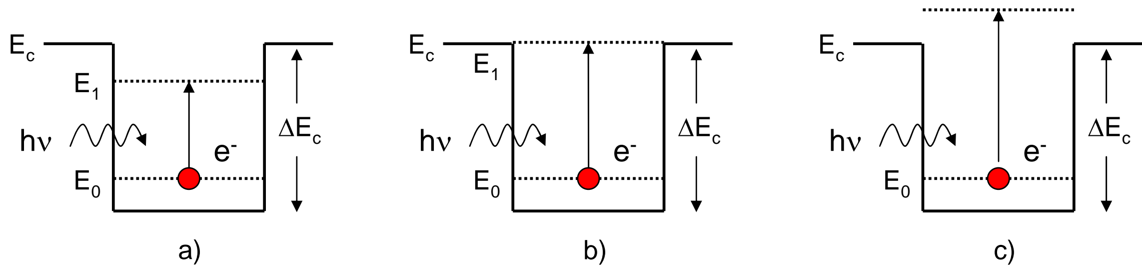

Figure 5.2: The (a) bound-to-bound, (b) bound-to-quasi-bound and (c) bound-to-continuum transitions of electrons in the conduction band are depicted.

bound-to-quasi-bound transition occurs between the ground state and an excited state at the upper limit of the quantum well. The bound-to-continuum transition occurs between a ground state to an unbounded state in the continuum.

Due to the selection rules in quantum mechanics, the absorption strength in these n-doped quantum wells is proportional to an incident photon´s electric field polarization component normal to the quantum well. If light is polarized in the x-y plane of the quantum well, the electron-photon coupling is zero [71]. But if light has a component parallel to the growth axis (z axis), then the electron-photon coupling is nonzero and intersubband transitions can be observed [72]. Because of the small thickness of the quantum wells, the measured optical absorption of the intersubband transition is usually very small. One way to increase the absorption intensity is to fabricate a waveguide through which the light will make multiple passes (see section optical properties). A detailed description of waveguide preparation is given in Ref. [70].

As already mentioned, it is possible to use wide band gap materials to detect light in the

infrared region from 1 to 3 μm. The epitaxial growth of two semiconductors with different band gaps allows the fabrication of such structures. This work focused on AlN/GaN quantum structures. The conduction band offsets provided in Fig. 5.3 are very important to achieve wavelengths shorter than 3 μm. Since the conduction band offsets in GaAs [73] and InP [74] is less than in AlN/GaN, the shortest detectable wavelengths with these materials are 3 and 8 μm, respectively. However, the large conduction band offset between c-GaN and c-AlN allows intersubband transitions in the IR range from 1 to 3 μm. Figure 5.3 shows the conduction band offset as a function of the Al mole

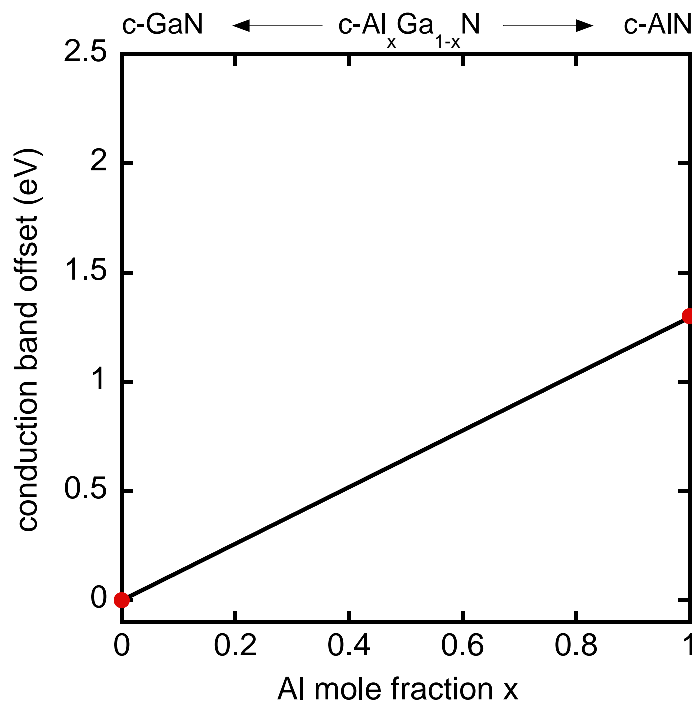

Figure 5.3: Band gap of $Al_xGa_{1-x}N$ and the conduction band offset of $GaN/Al_xGa_{1-x}N$ as a function of the Al mole fraction.

fraction. The conduction band offset is assumed to be 70 percent [56] of the total gap discontinuity for these calculations. The energy gap of $Al_xGa_{1-x}N$ is calculated by the following equation:

$$E_g(x) = xE_g(AlN) + (1 - x)E_g(GaN) \tag{5.1}$$

where $E_g(AlN)$, $E_g(GaN)$ are the band gaps of c-AlN and c-GaN (5.1 eV and 3.2 eV [7]), respectively, taking linear interpolation into account [75]. For this work only AlN/GaN quantum wells were grown to achieve the desired wavelength.
As mentioned before, the separation between the ground state E_0 and the first excited state E_1, which can be bound or unbound, corresponds to a particular wavelength. In the case of AlN/GaN quantum wells, the wavelength of interest is 1.55 μm which is used in optical communication. The only variable parameter for AlN/GaN quantum wells investigated for this work is the quantum well width. As reported by *Gmachl et al.* [76] intersubband transitions in the near infrared were observed when narrow wells and high aluminum compositions are used. Figure 5.4 shows the transition wavelength dependence of three quantum wells with decreasing well width (L_w) and identical conduction band

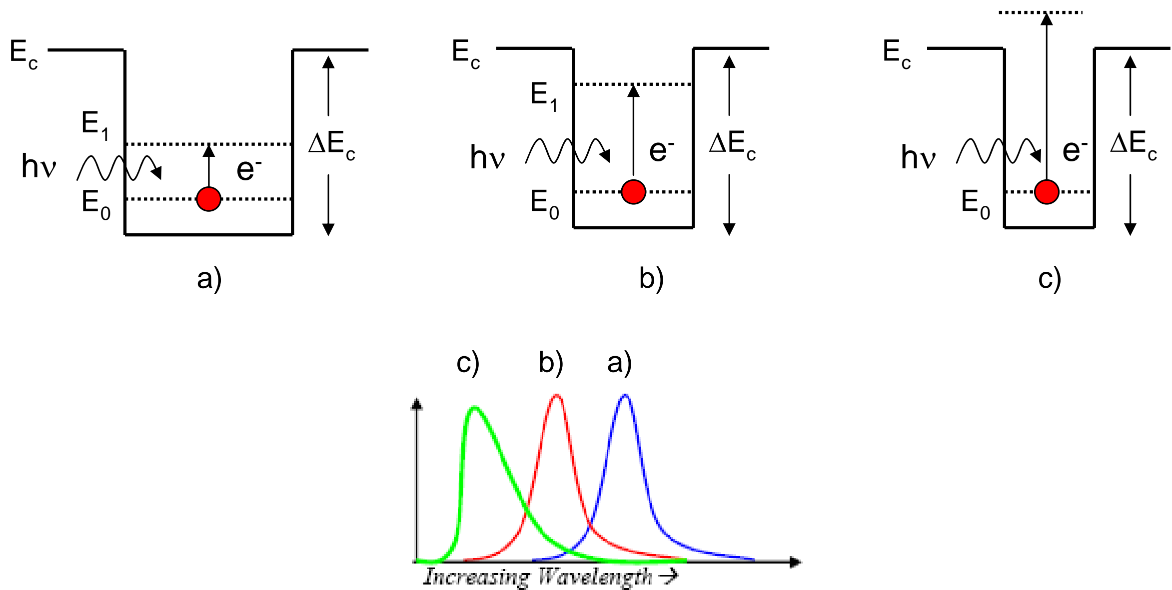

Figure 5.4: Schematic sketch of transitions in quantum wells with different well thicknesses. The blue curve indicates case (a) the red curve case (b) and the green curve case (c) [70].

offsets (ΔE_c). As the size of the quantum well is decreasing both E_0 and E_1 shift to higher energies, and the difference ΔE is increasing. This corresponds to decreasing wavelength needed to excite an electron to the first excited state. It should be noted that the green curve in Fig. 5.4 is slightly skewed with a tail, which is typical for a transition occuring outside the bounded states of the quantum well (bound-to-continuum transition). The other bound-to-bound transitions show a Lorentzian line shape [71].

The two major categories of infrared detectors are thermal and photonic (quantum) detectors. Quantum detectors operate on the principle of electron-photon interaction. Thus, these detectors are much faster than thermal detectors. For example *Iizuka et al.* [77] report an intersubband relaxation time of 150 fs in AlGaN/GaN MQWs. There are two basic processes involved in quantum detectors. Firstly, conduction electrons or electrons bound to the lattice atoms absorb light and thus get excited to higher energy levels. Secondly, the excited electrons are swept by an applied bias voltage and collected as an electrical signal. The quantum well infrared photodetector (QWIP) is based on intersubband transition, as shown in Fig. 5.5. The applied bias voltage shown on the right side in Fig. 5.5 causes the conduction band to bend and the excited state is than located near the edge of the barrier conduction band. Electrons in the ground state can

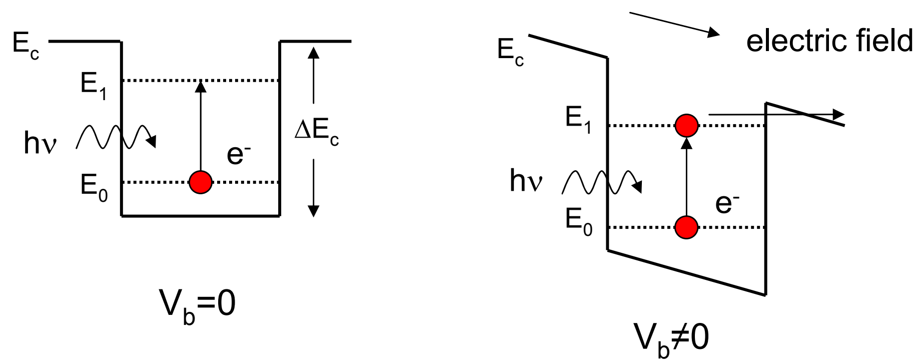

Figure 5.5: Typical quantum well design structure with two bound states. Quantum wells are shown without bias voltage on the left side and with applied bias voltage on the right side.

be excited by illuminating the sample with infrared light. They can tunnel through the barrier and then contribute to a photocurrent under the influence of the external field (bias voltage). The tunneling probability through the barrier is proportional to the bias voltage. The detector output signal is usually called a photocurrent. Photoconductivity measurements of a photodetector require fabricating a mesa so that electrodes can ba attached to the mesa and a bias voltage is applied. A typical mesa structure is shown in Fig. 5.6 where a quantum well structure is sandwiched between two ohmic contact layers.

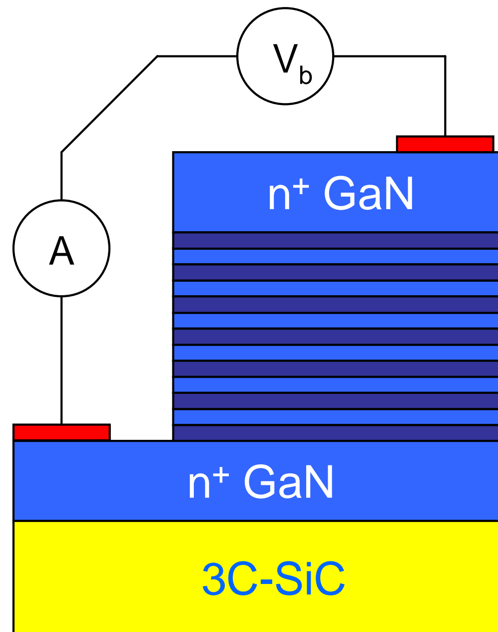

Figure 5.6: Mesa structure of a typical quantum well infrared photo detector. A bias voltage is supplied and a photocurrent is measured.

5.2 Growth of c-AlN/GaN superlattices

As a first step to test a material system´s suitability for application in IS-based devices, straightforward IS-absorption measurements are performed. As we are investigating the growth of c-AlN/GaN MQWs we are foremost interested in the observation of bound-to-bound transitions. In order to be able to observe bound-to-bound transitions in the range of 0.8 eV (1.55 μm), the transition energies were calculated using a square well self-consistent Poisson-Schrödinger model. The simulation was done for quantum wells embedded between 1.5 nm thick c-AlN barriers. We assume a 70:30 ratio of the conduction and valence band discontinuities [56]. The effective masses of c-GaN are $m_e = 0.15\ m_0$ [57] and $m_h = 0.8\ m_0$ and for c-AlN $m_e = 0.19\ m_0$ and $m_h = 1.2\ m_0$ [58], respectively. A net donor concentration of $N_D = 6 \times 10^{18}\ cm^{-3}$ was used for c-GaN

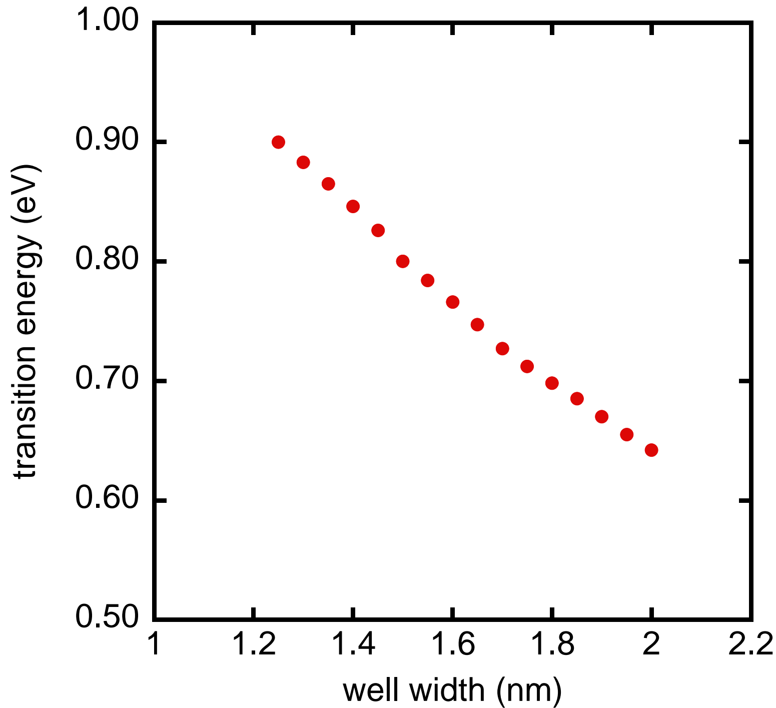

Figure 5.7: Transition energies of AlN/GaN multiple quantum well versus the QW thickness calculated by a self-consistent Poisson-Schrödinger model.

and $N_D = 7 \times 10^{19}\ cm^{-3}$ for c-AlN. These values are obtained by CV-measurements of thick GaN and AlN layers. Figure 5.7 shows the transition energies from E_0 to E_1 versus the QW thickness in the range of 1.3 nm to 2.1 nm. With increasing well thickness the transition energy is decreasing. A transition energy of 0.8 eV (1.55 μm) is expected for a QW thickness of 1.5 nm. Therefore we decided to realize the following structures. Figure 5.8 shows a schematic sketch of a c-AlN/GaN MQW structure.

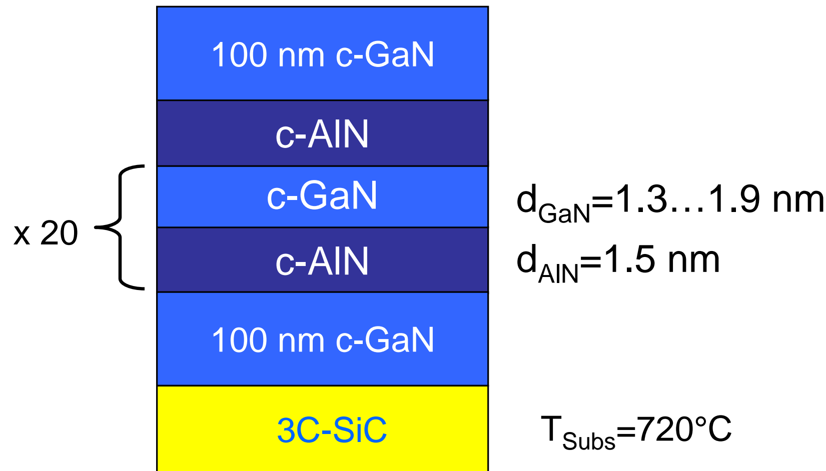

Figure 5.8: Schematic sketch of an AlN/GaN MQW structure for intersubband transitions. The thicknesses of the wells vary between 1.3 and 1.9 nm, the thickness of the barriers is 1.5 nm.

A 100 nm thick c-GaN buffer was deposited on a 3C-SiC substrate using the growth process described in chapter 3 and Ref. [31]. Then a 20 period AlN/GaN superlattice was grown with well widths ranging from 1.3 nm to 1.9 nm and a barrier width of 1.5 nm. The growth temperature was 720°C. We fabricated four samples with varying QW thicknesses to see the shift in transition energy. After each layer the growth was stopped for 30 seconds to allow excess metal to evaporate from the surface. The RHEED intensity was recorded versus time when the superlattice was started. The shutters were opened and closed using a computer program to guarantee the same thickness of the wells and the barriers.

A typical RHEED timescan of sample 1518 after opening of both the Al and the N shutter is shown in Fig. 5.9. Clear RHEED oscillations of c-AlN are seen after opening

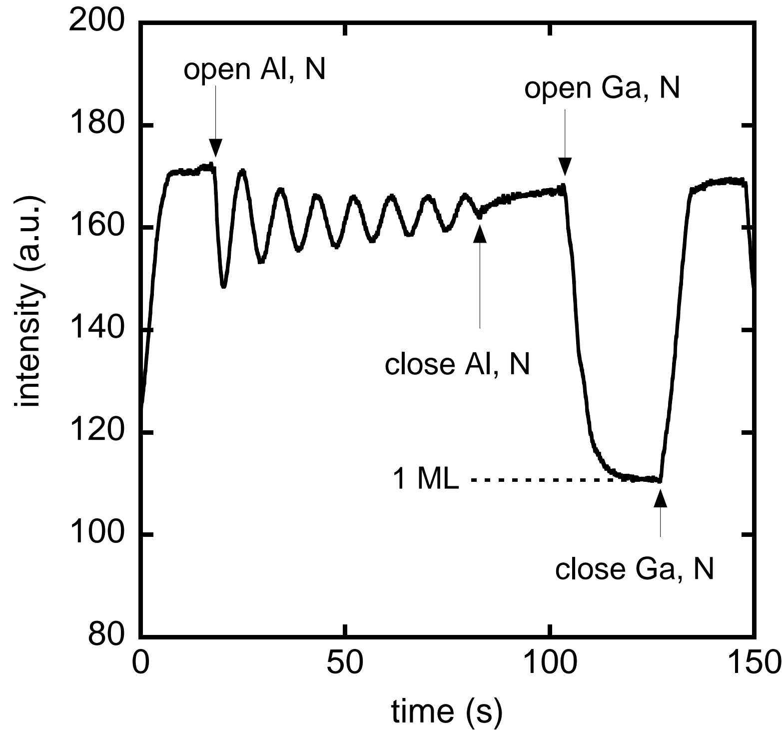

Figure 5.9: RHEED timescan of sample 1518 on an extended scale. The shutter sequence and the coverage of 1 ML during c-GaN growth is indicated in the figure.

the Al and N shutter. Using the number of deposited AlN monolayers a barrier thickness of 1.5 nm was calculated, assuming a lattice constant of $a_{AlN} = 4.38$ $\AA$. The GaN wells were grown for a certain time (depending on the well thickness) taking a growth rate of 210 nm/h into account. This growth rate was obtained using optical interference spectroscopy with thick c-GaN layers. After a growth interruption of 20 sec. we opened the Ga and N shutter simultaniously. The RHEED intensity decreases and saturates at a Ga-coverage of 1 ML. After closing the Ga an N shutter the intensity increases and saturates indicating a Ga free surface. The growth rate of the AlN barrier observed by RHEED oscillation is 87 nm/h. We found that the growth rate of AlN is lower than that of GaN, which is due to nitrogen rich growth conditions. Nitrogen-rich growth conditions

are required due to the small growth window for c-AlN at 720°C. Similar results were obtained by *Heying et al.* [79] for growth of GaN. By comparing the RHEED timescan

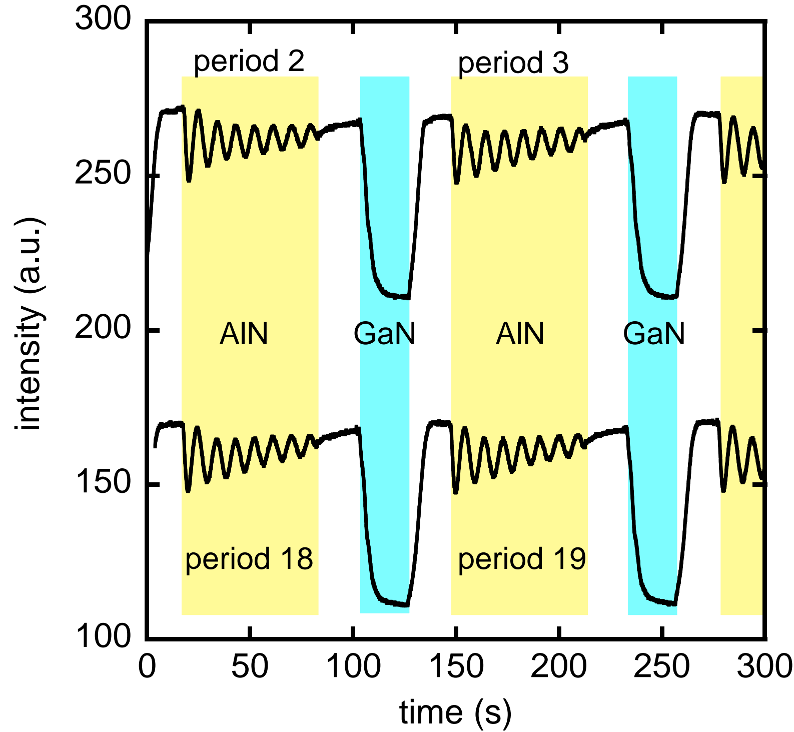

Figure 5.10: RHEED intensity versus time during the growth of an AlN/GaN superlattice of sample 1518. The Fig. shows the RHEED intensities of period 2 and 3 and of period 18 and 19. The shaded area indicates the growth of the individual layer. The scans are vertically shifted for clarity.

obtained during growth of different periods we found a growth mode which is highly reproducible as shown in Fig. 5.10. The Fig. shows the RHEED intensity versus time for the second and the third period and for periods 18 and 19. For clarity the time scans of period 18 and 19 has been shifted both in time and in position in Fig. 5.10. The shaded area indicates the growth of the individual layer. These timescans are identical revealing a high reproducible growth process within the superlattice.

5.3 Structural properties of AlN/GaN SLs

The structural properties were investigated by HRXRD and AFM. The ω-2Θ scan of sample 1518 is shown in Fig. 5.11 together with a simulation using a dynamic scattering model [47]. The reflexes of the 3C-SiC substrate, of the c-GaN buffer as well as of two superlattice peaks are clearly resolved.

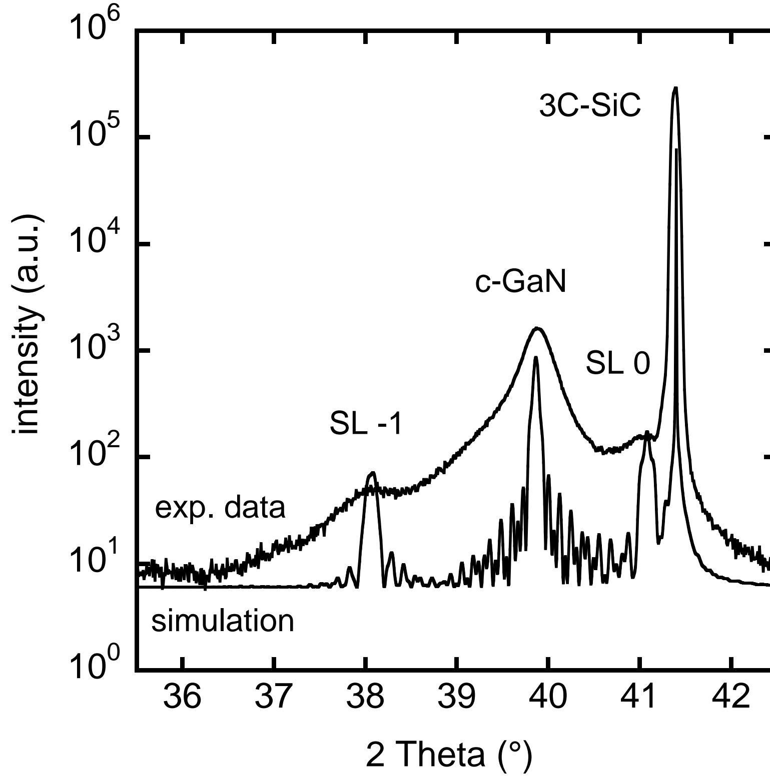

Figure 5.11: ω-2Θ scan and simulated data of the (002) reflex of sample 1518. The sample consists of a 20-fold AlN/GaN MQW structure. The simulation reveals a barrier thickness of 1.35 nm and a QW thickness of 1.75 nm.

The thickness of a SL period (consisting of one QW and one barrier) is given by eq.

$$d = \frac{n \cdot \lambda}{2(\sin\Theta_m - \sin\Theta_n)} \tag{5.2}$$

where Θ_m and Θ_n are the positions of the superlattice peaks and λ is the wavelength

of the X-ray beam. From the difference of the superlattice peaks a periodicity of 3.1 nm was calculated [16]. Due to the unknown strained lattice parameter of AlN the QW and barrier thicknesses were determined from dynamic simulation. The thickness is 1.75 nm for the QW and 1.35 nm for the barrier. These values differ slightly from the calculated data obtained by RHEED oscillation period for the AlN barrier. The thickness of the AlN barrier is thinner than estimated, which can be explained by the strain of the AlN layers. Strain reduces the vertical lattice constant which results in a smaller lattice parameter than included in our calculations. The QWs are thicker which is due to uncertainties in growth rate calculations and a second reason may be growth rate fluctuation caused by our plasma source.
The surface roughness of these structures was investigated by AFM. The RMS roughness of sample 1518 is 2.6 nm on a 5×5 μm scan area, which is in the order of the best values reported for bulk c-GaN layers (see Fig. 3.8). The QW thicknesse, the FWHM of the X-ray rocking curves and the RMS roughness of the investigated structures are summarized in table 1

sample number	QW thickness (nm)	RMS roughness (nm)	FWHM X-ray (arcmin)
1518	1.75	2.6	36
1544	1.6	4.2	36
1545	1.65	5.9	37
1547	2.1	3.2	36

Table 1: Structural parameters of AlN/GaN MQW samples.

The surface roughness of sample 1518 is the lowest within this series of samples. The FWHMs of the XRD rocking curve are identival for all samples.

5.4 Optical properties of AlN/GaN SLs

The absorption measurements were performed in a waveguide geometry at the University of Arkansas, group of Prof. Dr. M.O. Manasreh. The samples were cut into 5 mm × 2 mm wide pieces. The 45 degree facets were fabricated by lapping using various grades of lapping material. Details are given in Ref. [70]. Figure 5.12 shows the SEM image of a waveguide with two 45 degree facets. Figure 5.13 illustrates the propagation of light through the waveguide. The angles of total reflection for the SiC-air and GaN-air interfaces are 23.09° and 25.3°, respectively.

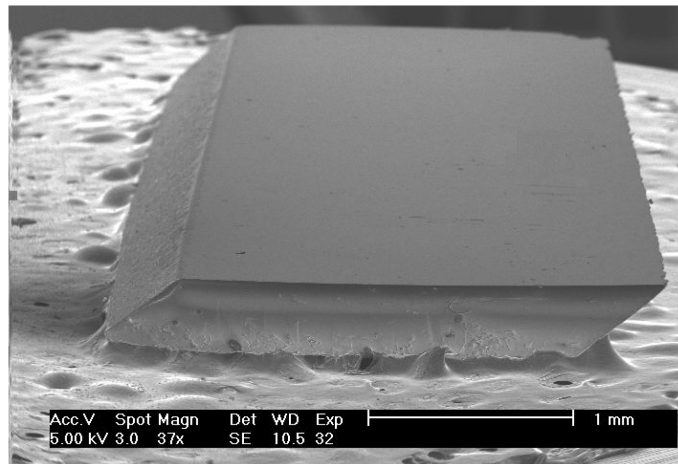

Figure 5.12: An SEM image of a waveguide with approximately 2 mm width and 5 mm length [70].

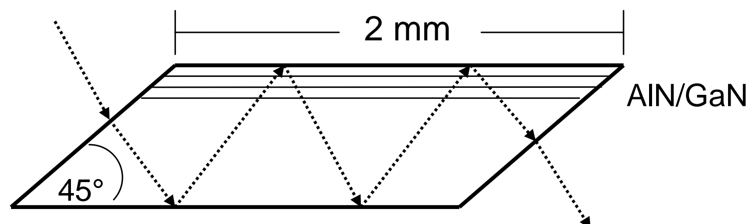

Figure 5.13: Illustration of light propagating through a waveguide.

The optical measurements were performed using a *Bomen DA8 FTIR* spectrometer. The light was detected by a HgCdTe detector, cooled by liquid nitrogen. The optical range for this detector is 1 to 12 μm (0.1 to 1.24 eV) and has a detectivity greater than 4×10^{10} $cmHz^{1/2}W^{-1}$ [70].

The room-temperature optical absorbance spectra of samples 1518, 1544, 1545, 1547 and a 3C-SiC substrate are plotted in Fig. 5.14. All four samples show a clear absorption peak in the range of 0.6 eV to 0.8 eV (1.6 μm to 2 μm). These structures consist of AlN/GaN MQWs with a well width between 1.6 and 2.1 nm. The absorption below 0.4 eV (3.2 μm) is due to absorption bands from the 3C-SiC substrate. The spectra are vertically shifted for clarity. Figure 5.15 shows the absorbance of the same four samples

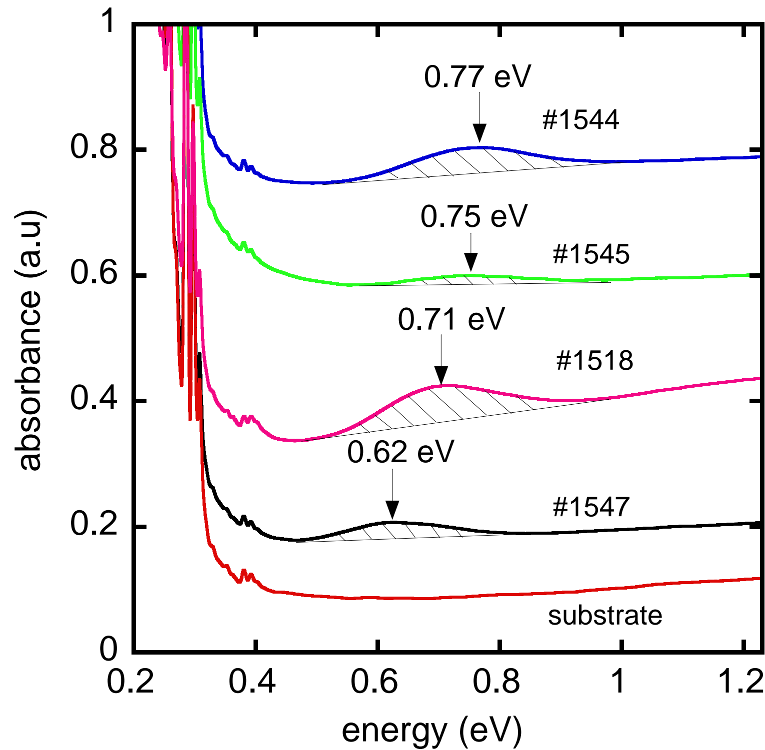

Figure 5.14: Room-temperature absorbance spectra of 4 AlN/GaN MQW structures and of a substrate. Absorption was observed in the range of 0.6 eV to 0.8 eV (1.6 μm to 2 μm). The spectra are vertically shifted for clarity.

in the spectral range from 0.5 eV to 1.1 eV (1.1 μm to 2.5 μm) with the absorbance of

the substrate subtracted. A shaded area indicates the communication wavelength of 0.8 eV (1.55 μm). The IS-transition of sample 1544 is nearly located at the favored wavelength of 0.8 eV (1.55 μm). The lineshape of the absorption of samples 1518 and 1544

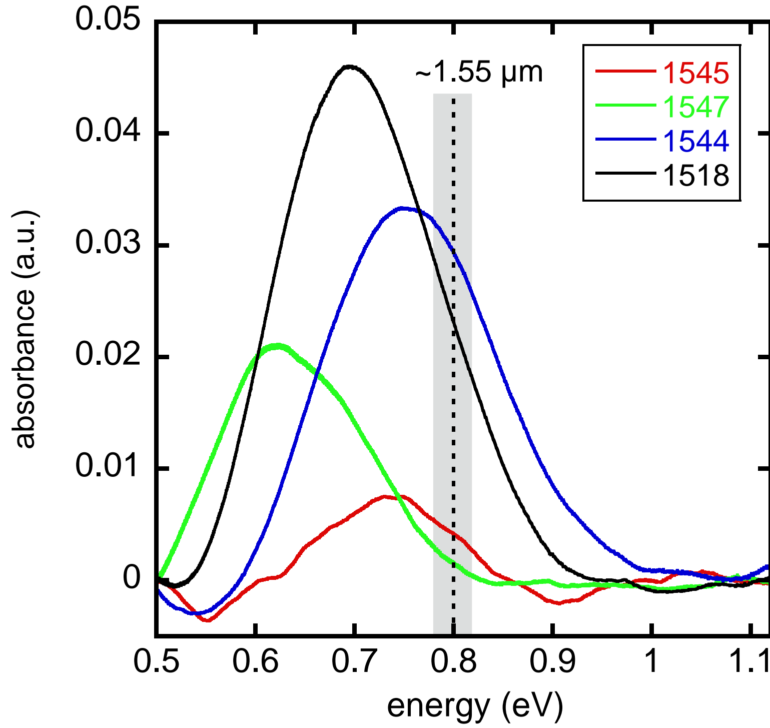

Figure 5.15: Intersubband absorption of four AlN/GaN MQWs. The spectra are plotted after subtraction of the substrate background in the spectral range between 0.5 eV and 1.1 eV (1.1 μm and 2.5 μm). A shaded area indicates the wavelength of 1.55 μm. The FWHM of all samples is about 200 meV.

is symmetrical which is an indicator for a bound-to-bound intersubband transition. The lineshape of sample 1545 and 1547 is asymmetrical, which is most likely due to interface fluctuations in the quantum well. The absorption peak energy is inverse proportional to the quantum well width and lies between 0.6 eV and 0.8 eV (1.6 μm to 2 μm). The line width (FWHM) of the absorption peaks is about 200 meV. The FWHM is larger than in hexagonal AlGaN/GaN MQW structures (130 meV) [80]. This is most likely related to the interface roughness of the AlN/GaN interfaces.

In the following I discuss the transition energies of sample 1518 by comparing the experimental data with theoretical calculations. Figure 5.16 shows a simulation of the conduction band of sample 1518. In this calculation a square well self-consistent Poisson-Schrödinger model [55] was used with the parameters given above and in table 1. For simplicity we only used five quantum wells to calculate the transition energies. At

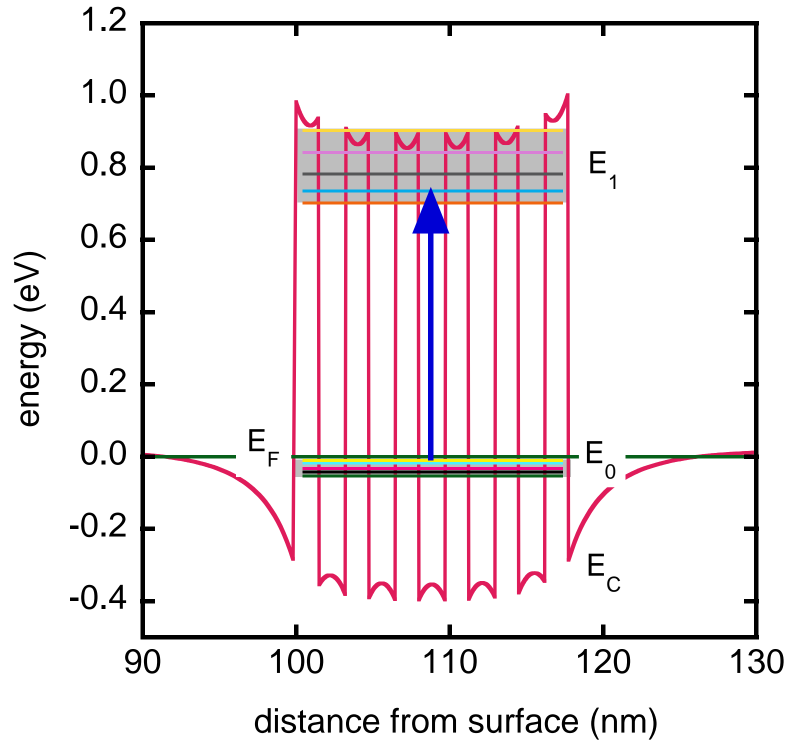

Figure 5.16: Simulation of the conduction band of sample 1518. Two bounded states are observed within the quantum well. The shaded area indicates the distribution of the first excited state E_1.

least ten quantized energy levels were observed in this structure. The first five states are located below the Fermi energy. They form a miniband due to the overlap of the wave functions. The excited states also form a miniband above 0.7 eV. The transition energy is 0.712 eV (1.76 μm) as indicated by an arrow in the figure. The thickness of the quantum well used for this calculation was 1.75 nm. This is in good agreement with the experimental results given in Fig. 5.15. The miniband of the first excited state has

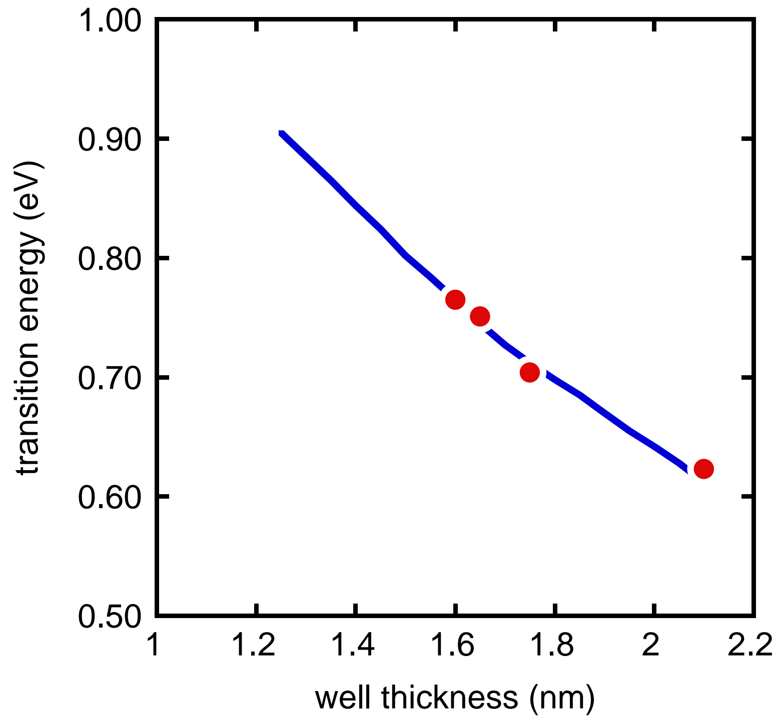

Figure 5.17: Transition energies of AlN/GaN multiple quantum wells versus the QW thickness as shown in Fig. 5.7. The experimental data show good agreement with the calculated data.

a distribution of about 200 meV and is indicated by the shaded area in Fig. 5.16, which is in good agreement to the observed line widths in the absorbance spectra. Figure 5.17 shows the calculated and the measured transition energies as a function of the well width in the range between 1.3 nm an 2.1 nm. The experimental data show excellent agreement with the calculated values. To reach the target wavelength of 1.55 μm thinner quantum wells are required, which will be one of the next steps for epitaxy.

20 period c-AlN/GaN SL structures grown by MBE serve as first demonstration that IS-transitions in the communication wavelength range can be achieved with metastable cubic group III-nitrides. This result is an extremely important milestone towards the demonstration of a high performance intersubband detector at the telecommunication wavelength of 1.55 μm.

6 Conclusion

Metastable cubic GaN layers were grown on free standing 3C-SiC (001) substrates. The main focus of this work was the investigation of the growth process of cubic III-nitrides by plasma assisted molecular beam epitaxy to reduce the surface and the interface roughness. We studied the adsorption of Ga on c-GaN using *in situ* reflection high energy electron diffraction. The drop of the RHEED intensity after growth was started had been calibrated to allow direct measurements of the Ga-coverage at growth conditions with an accuracy of 0.1 ML. The roughness of cubic GaN was significantly reduced by growth under controlled Ga-excess conditions. A minimum RMS roughness of 2.5 nm was achieved using a Ga-coverage of 1 ML during c-GaN growth. Cubic GaN layers grown under these conditions have narrow x-ray (002) rocking curves (16 arcmin) indicating also a low density of extended defect in these layers. Our data show that the epitaxy of c-GaN with high structural quality is only possible if the amount of excess Ga on the surface is monitored with high accuracy during growth.

Cubic $Al_{0.15}Ga_{0.85}N$/GaN single and multiple quantum wells were grown on top of c-GaN buffer layers. During growth of $Al_{0.15}Ga_{0.85}N$/GaN QWs clear RHEED oscillations were observed allowing a stringent control of the growth rate and indicating a two-dimensional growth of the respective layers. The peak energy of the emission from our cubic $Al_{0.15}Ga_{0.85}N$/GaN QWs follows the square-well Poisson-Schrödinger model and demonstrates the absence of polarization-induced electrical fields. The FWHM of c-QW luminescence is almost identical to values reported for nonpolar hexagonal AlGaN/GaN quantum wells. Our results obtained with quantum wells grown on 3C-SiC substrates indicate that the well-known thermodynamic metastability of the cubic nitrides does not

necessarily limit their application for polarization-free structures.

First intersubband transitions in 20 period c-AlN/GaN multiple quantum wells were observed in the near infrared region. The c-GaN well widths were estimated from X-ray simulations. 1.6 nm to 2.1 nm thick quantum wells show intersubband transitions between 1.6 μm and 2.1 μm. Simulation of transition energy using self-consistent Poisson-Schrödinger model show excellent agreement to experimental data. The absence of built-in fields in these structures will simplify the design of polarization-free intersubband devices.

7 Appendix

Table A.1 gives a short overview of the physical properties of c-GaN and c-AlN. The parameter for the ternary compounds are calculated by linear interpolation of the binary compounds.

Parameter	c-GaN	c-AlN	Reference
lattice constant (Å)	4.52	4.38	[81] [82]
Band gap (eV)	3.2	5.1	[58]
effective conduction band mass			
$\frac{m_e}{m_0}$	0.15	0.19	[58]
effective hole mass			
$\frac{m_{hh}}{m_0}$	0.8	1.2	[58]
$\frac{m_{lh}}{m_0}$	0.18	0.33	[58]
Deformation Potential (eV)			
a_c	-2.77	-6.8	[83] [84]
b	-2.67	-1.5	[84] [85]
Elastic coefficients (GPa)			
c_{11}	296	304	[84]
c_{12}	154	152	[84]

The Poisson ratio which is defined as $\nu = \frac{c_{11}}{c_{11}-c_{12}}$ was used to calculate the strain and the transition energies in our AlGaN/GaN heterostructures.

Bibliography

[1] S. Nakamura, and G. Fasol, *The Blue Laser Diode* (Springer, Berlin, 1997)

[2] F.M. Steranka, J. Bhat, D. Collins, L. Cook, M.G. Craford, R. Fletcher, N. Gardner, P. Grillot, W. Goetz, M. Keuper, R. Khare, A. Kim, M. Krames, G. Harbers, M. Ludowise, P.S. Martin, M. Misra, G. Mueller, R. Mueller-Mach, S. Rudaz, Y.-C. Shen, D. Steigerwald, S. Stockman, S. Subramanya, T. Trottier, and J.J. Wierer, Phys. stat. sol. (a)**194**, 380 (2002)

[3] J.S. Im, H. Kollmer, J. Off, A. Sohmer, F. Scholz, and A. Hangleiter, Phys. Rev. B **57**, R9435 (1998)

[4] M.D. Craven, P. Waltereit, F. Wu, J.S. Speck, and S.P. DenBaars, Jpn. J. Appl. Phys. **42**, L235 (2003)

[5] P. Waltereit, O. Brandt, A. Trampert, H.T. Grahn, J. Menninger, M. Ramsteiner, M. Reiche, and K.H. Ploog, Nature (London) **406**, 3850 (2000)

[6] H.M. Ng, Appl. Phys. Lett. **80**, 4369 (2002)

[7] D.J. As, in *Optoelectronic Properties of Semiconductors and Superlattices*, series editor M.O. Manasreh, (Taylor&Francis Books, Inc., New York, 2003), Vol. **19** chapter 9, pp. 323-450

[8] D.J. As, S. Potthast, J. Schörmann, S.F. Li, K. Lischka, H. Nagasawa, and M. Abe, Materials Science Forum Vols. **527-529**, 1489 (2006)

[9] J. Bai, T. Wang, and S. Sakai, J. Appl. Phys. **88**, 4729 (2000)

[10] M.B. Nardelli, K. Rapcewicz, and J. Bernholc, Appl. Phys. Lett. **71**, 3135 (1997)

[11] S.F. Chichibu, T. Onuma, T. Aoyama et al., J Vac. Sci. Technol. B **21**, 1856 (2003)

[12] M.A. Herman, H. Sitter *Molecular Beam Epitaxie: fundamentals and current status*, Springer Verlag, Berlin 1989

[13] W. Braun, *Applied RHEED* (Springer Verlag, Heidelberg, 1999)

[14] W.L. Bragg, Proc. Cambridge Phil. Soc. 17, **43** (1913)

[15] B.E. Warren, *X-Ray diffraction*, Dover, New York 1986

[16] G. Bauer, and W. Richter, *Optical characterization of Epitaxial Semiconductor Layers*, (Springer Verlag, Berlin, Heidelberg, New York 1996)

[17] A. Khartchenko, *In situ X-Ray diffraction*, Ph.D. thesis, Universität Paderborn 2003

[18] Fa. Topometrix, Manual, TMX2000-System, Darmstadt (1993)

[19] L. Pavesi, and M. Guzzi, J. Appl. Phys. **75**, 4779 (1994)

[20] P.Y. Yu, and M. Cardona, *Fundamentals of Semiconductors*, (Springer Verlag, Berlin, Heidelberg 1996)

[21] C.F. Klingshirn, *Semiconductor Optics*, (Springer Verlag, Berlin, Heidelberg 1995)

[22] D. Schikora, M. Hankeln, D.J. As, K. Lischka, T. Litz, A. Waag, T. Buhrow, and F. Henneberger, Phys. Rev. B **54**, R8381 (1996)

[23] D.J. As, F. Schmilgus, C. Wang, B. Schöttker, D. Schikora, and K. Lischka, Appl. Phys. Lett. **70**, 1311 (1997)

[24] Z.X. Liu, A.R. Goni, K. Syassen, H. Siegle, C. Thomsen, B. Schöttker, D.J. As, and D. Schikora, J. Appl. Phys. **86**, 929 (1999)

[25] G. Ramirez-Florez, H. Navarro-Contreras, A. Lastras-Martinez, R.C. Powell, and J.E. Greene, Phys. Rev. B **50**, 8433 (1994)

[26] J.E. Northrup, J. Neugebauer, R.M. Feenstra, and A.R. Smith, Phys. Rev. B **61**, 9932 (2000)

[27] G. Koblmüller, J. Brown, R. Averbeck, H. Riechert, P. Pongratz, and J.S. Speck, Appl. Phys. Lett. **86**, 041908 (2005)

[28] O. Brandt, Y.J. Sun, L. Däweritz, and K.H. Ploog, Phys. Rev. B **69**, 165326 (2004)

[29] G. Feuillet, H. Hamaguchi, K. Ohta, P. Hacke, H. Okumura, and S. Yoshida, Appl. Phys. Lett. **70**, 1025 (1997)

[30] J. Neugebauer, Z. Zywietz, M. Scheffler, J.E. Northrup, and C.G. Van der Walle, Phys. Rev. Lett. **80** 3097 (1998)

[31] J. Schörmann, S. Potthast, D.J. As, and K. Lischka, Appl. Phys. Lett. **90**, 041918 (2007)

[32] B. Schöttker *Molecular Beam Epitaxie and Characterization of doped and undoped cubic GaN Layers*, Ph.D. thesis, Shaker Verlag Aachen, 1999

[33] H. Nagasawa, K. Yagi, T. Kawahara, and N. Hatta, Mat. Sci. For. **433-436**, 3-8 (2002)

[34] G. Mula, C. Adelmann, S. Moehl, J. Oullier, and B. Daudin, Phys. Rev. B **64**, 195406 (2001)

[35] C. Adelmann, J. Brault, D. Jalabert, P. Gentile, H. Mariette, G. Mula, and B. Daudin, J. Appl. Phys. **91**, 9638 (2002)

[36] N. Gogenau, E. Sarigiannidou, E. Monroy, S. Monnoye, H. Mank, and B. Daudin, Appl. Phys. Lett. **85**, 1421 (2004)

[37] J. Neugebauer, T.K. Zywietz, M. Scheffler, J.E. Northrup, H. Chen, and R.M. Feenstra, Phys. Rev. Lett. **90**, 056101 (2003)

[38] A. Nagayama, H. Sawada, E. Takuma, R. Katayama, K. Onabe, H. Ichinose, and Y. Shiraki, Inst. Phys. Conf. Ser. **170**, 749 (2002)

[39] H. Okumura, K. Ohta, G. Feuillet, K. Balakrishnan, S. Chichibu, H. Hamaguchi, P. Hacke, and S. Yoshida, J. Cryst. Growth **113**, 178 (1997)

[40] B. Daudin, G. Feuillet, J. Hübner, Y. Samson, F. Widmann, A. Philippe, C. Bru-Chevallier, G. Guillot, E. Bustarret, G. Bentoumi, and A. Deneuville, J. Appl. Phys. **84**, 2295 (1998)

[41] J.E. Ayers, J. Appl. Phys. **78**, 3724 (1995)

[42] T. Frey, *Cubic III-Nitride Quantum Structures Grown by Molecular Beam Epitaxy*, Ph.D. thesis, Universität Paderborn 2000

[43] W.A. Harrison, *Electronic Structure and the Properties of Solids*, Dover, New York, 1980

[44] J. Schörmann, *Herstellung und strukturelle Charakterisierungvon kubischen AlGaN/GaN Heterostrukturen*, Diplomarbeit, Universität Paderborn 2003

[45] S. Potthast, *Growth and Characterization of cubic AlGaN/GaN based Devices*, Ph.D. thesis, Universität Paderborn 2007

[46] M.E. Sherwin, T.J. Drummond, J. Appl. Phys **69**, 8423 (1991)

[47] V. Holy, U. Pietsch, and T. Baumbach, *High resolution X-ray scattering from thin films and multilayers*, (Springer Verlag, Berlin, 1999)

[48] J. Schörmann, S. Potthast, M. Schnietz S. Li, D.J. As, and K. Lischka, phys. stat. sol. (c) **3**, 1604 (2006)

[49] D.J. As, S. Potthast, U. Köhler, A. Khartchenko, and K. Lischka, Mater. Res. Soc. Symp. **743**, L5.4 (2003)

[50] Y.P. Varshni, Physica **34**, 149 (1967)

[51] M.D. Craven, P. Waltereit, J.S. Speck, and S.P. DenBaars, Appl. Phys. Lett. **84**,496 (2004)

[52] J. Bai, T. Wang, P. Comming, P.J. Parbrook, J.P.R. David, and A.P. Cullis, J. Appl. Phys. **99**, 023513 (2006)

[53] V. Dumitru, *Physics and Technology of Nitride Lasers*, Ph.D. thesis, Universität Stuttgart (2004)

[54] N. Grandjean, B. Damilano, S. Dalmasso, M. Leroux, M. Laügt, and J. Massies, J. Apll. Phys. **86**, 3724 (1999)

[55] I.H. Tan, G.L. Snider, L.D. Chang, and E.L. Hu, J. Appl. Phys. **68**, 4071 (1990)

[56] A. Teke, S. Dogan, F. Yun, M.A. Reshchikov, H. Lee, X.Q. Liu, H. Morkoc, S.K. Zhang, W.B. Wang, and R.R. Alfano, Solid-State Electron. **47**, 1401 (2003)

[57] M. Fanciulli, T. Lei, and T. Moustakas, Phys. Rev. B **48**, 15144 (1993)

[58] S. Pugh, D.J Dugdale, S. Brand, and R.A. Abram, Semicond. Sci. Techno. **14**, 23 (1999)

[59] J. Schörmann, S. Potthast, D.J. As, and K. Lischka, Appl. Phys. Lett. **89**, 131910 (2006)

[60] N. Suzuki and N. Iizuka, Jpn. J. Appl. Phys. Part 2 **36**, L1006 (1999)

[61] N. Suzuki and N. Iizuka, Jpn. J. Appl. Phys., Part 2 **37**, L369 (1998)

[62] N. Suzuki, N. Iizuka, and K. Kaneko, Jpn. J. Appl. Phys., Part 1 **42**, 132 (2003)

[63] D. Hofstetter, E. Baumann, F.R. Giorgetta, M. Graf, M. Maier, F. Guillot, E. Bellet-Amalric, and E. Monroy, Appl. Phys. Lett. **88**, 121112 (2006)

[64] E. Baumann, F.R. Giorgetta, D. Hofstetter, H. Lu, X. Chen, W.J. Schaff, L.F. Eastman, S. Golka, W. Schrenk, and G. Strasser, Appl. Phys. Lett. **87**, 191102 (2005)

[65] D. Hofstetter, S.S. Schad, H. Wu, W.J. Schaff, and L.F. Eastmen, Appl. Phys. Lett. **83**, 572 (2003)

[66] Q. Zhou, J. Chen, B. Pattada, M.O. Manasreh, F. Xiu, S. Puntigan, L. He, K.S. Ramaiah, and H. Morkoç, J. Appl. Phys. **93**, 10140 (2003)

[67] K. Kishino, A. Kikuchi, H. Kanazawa, and T. Tachibana, Appl. Phys. Lett. **81**, 1234 (2002)

[68] C. Gmachl, H.M. Ng, and A.Y. Cho, Appl. Phys. Lett. **79**, 1590 (2001)

[69] H.M. Ng, C. Gmachl, J.D. Heber, J.W.P. Hsu, S.N.G. Chu, and A.Y. Cho, phys. stat. sol. (b) **234**, No. 3, 871 (2002)

[70] E.A. Decuir Jr., *Characterization of Intersubband Transitions in $Al_xGa_{1-x}N/GaN$ multiple quantum well structures: For near infrared detector application*, University of Arkansas 2005

[71] O. Manasreh, *Semiconductor Heterojunctions and Nanostructures*, McGraw-Hill Professional 2005

[72] A. Rogalski, J. Appl. Phys. **93**, 4355 (2003)

[73] J. Faist, F. Capasso, D.L. Sivco, A.L. Hutchinson, S.N.G. Chu, and A.Y. Cho, Appl. Phys. Lett. **72**, 680 (1998)

[74] C. Fabry, and A. Perot, Ann. Chim. Phys. **16**, 115 (1899)

[75] A. Nakadaira, and H. Tanaka, Appl. Phys. Lett. **70**, 2720 (1997)

[76] C. Gmachl, H.M. Ng, S.-N.G. Chu, and A.Y. Cho, Appl. Phys. Lett. **77**, 3722 (2000)

[77] N. Iizuka, K. Kaneko, N. Suzuki, T. Asano, S. Noda, O. Wada, Appl. Phys. Lett. **77**, 648 (2000)

[78] H. Morkoç, *Nitride Semiconductors and Devices*, (Springer-Verlag, New York, 1999)

[79] B. Heying, I. Smorchkova, C. Poblenz, C. Elsass, P. Fini, S. Den Baars, U. Mishra, and J.S. Speck, Appl. Phys. Lett. **77**, 2885 (2000)

[80] E.A. Decuir Jr., E. Fred, B.S. Passmore, A. Muddasani,M.O. Manasreh, J. Xie, H. Morkoç, M.E. Ware, and G.J. Salamo, Appl. Phys. Lett. **89**, 151112 (2006)

[81] I. Petrov, E. Mojab, R.C. Powell and J. E. Greene, Appl. Phys. Lett. **60**, 2491 (1992)

[82] T. Lei, M. Fanciulli, R.J. Molnar, T.D. Moustakas, R.J. Graham, and J. Scanlon, Appl. Phys. Lett. **59**, 944 (1991)

[83] C.G. van de Walle and J. Neugebauer, Appl. Phys. Lett. **70** (19), 2577 (1997)

[84] K. Kim, W.R.L. Lambrecht, and B. Segall, Phys. Rev. B **53**, 16310 (1996)

[85] S.H. Park, and S.L. Chuang, J. Appl. Phys. **87**, 353 (2000)

List of samples

Sample No	Date of growth	Structure	Al content
1117	12.12.03	AlGaN/GaN MQW	0.25
1132	05.02.04	AlGaN/GaN SQW	0.15
1138	12.02.04	AlGaN/GaN SQW	0.15
1143	16.02.04	AlGaN/GaN MQW	0.15
1204	07.06.04	GaN	
1221	15.07.04	GaN	
1286	15.12.04	GaN	
1287	16.12.04	GaN	
1304	07.02.05	GaN	
1310	12.12.12	GaN	
1314	12.12.12	AlGaN/GaN HS	0.3
1360	23.05.05	GaN	
1372	21.06.05	AlGaN/GaN MQW	0.3
1397	25.08. 05	AlGaN/GaN	0.33
1398	26.08.05	AlGaN/GaN	0.49
1403	02.09.05	AlGaN/GaN	0.57
1426	11.10.05	AlGaN/GaN	0.14 0.25 0.38 0.67
1436	31.10.05	AlGaN/GaN	0.18 0.32 0.52

Sample No	Date of growth	Structure	Al content
1437	02.11.05	AlGaN/GaN	0.8
1441	10.11.05	AlGaN/GaN	0.74
1447	19.11.05	AlGaN/GaN	0.48
1448	20.11.05	AlGaN/GaN	0.54
1452	24.11.05	AlGaN/GaN	0.54
1455	27.11.05	AlGaN/GaN	0.65
1459	01.12.05	AlGaN/GaN	0.82
1518	21.11.06	AlN/GaN MQW	
1544	05.02.07	AlN/GaN MQW	
1545	06.02.07	AlN/GaN MQW	
1547	08.02.07	AlN/GaN MQW	

Publication List

1. A. Pawlis, D.J. As, D. Schikora, **J. Schörmann**, and K. Lischka, *Photonic devices based on wide gap semiconductors for room temperature polariton emission*
phys. stat. sol. (c), **1**, 202 (2004)

2. S. Li, **J. Schörmann**, A. Pawlis, D.J. As, and K. Lischka, *Cubic InGaN/GaN multiple quantum wells and AlGaN/GaN Bragg reflectors for green resonant cavity LED*
in IEEE Proceedings SIMC-XIII, Bejing, p.61 (2004)

3. S. Li, **J. Schörmann**, A. Pawlis, D.J. As, K. Lischka, *Cubic InGaN/GaN multi-quantum wells and AlGaN/GaN distributed Bragg reflectors for application in resonant cavity LEDs*
Microelectronics Journal **36**, 963 (2005)

4. M. Abe, H. Nagasawa, S. Potthast, J. Fernandez, **J. Schörmann**, D.J. As, and K. Lischka, *Cubic GaN/AlGaN HEMTs von 3C-SiC substrate for normally-off operation*
IEICE Transactions on Electronics, **E89**-C (7), 1057 (2006)

5. D.J. As, S. Potthast, J. Fernandez, **J. Schörmann**, and K. Lischka, *Ni Schottky diodes on cubic GaN*
Appl. Phys. Lett. **88**, 1521112 (2006)

6. J. Schörmann, S. Potthast, M. Schnietz, S.F. Li, D.J. As, and K. Lischka, *Growth of ternary and quaternary cubic III-nitrides on 3C-SiC substrates*
phys. stat. sol. (c) **3**, 1604 (2006)

7. S. Potthast, **J. Schörmann**, J. Fernandez, D.J. As, K. Lischka, H. Nagasawa, M. Abe, *Two-dimensional electron gas in cubic* $Al_xGa_{1-x}N/GaN$ *heterostructures*
phys. stat. sol. (c) **3**, 2091 (2006)

8. D.J. As, S. Potthast, **J. Schörmann**, S.F. Li, K. Lischka, H. Nagasawa, M. Abe, *Molecular beam epitaxy of cubic group III-Nitrides on free-standing 3C-SiC substrates*
Matrials Science Forum Vols. **527-529**, 1489 (2006)

9. **J. Schörmann**, S. Potthast, D.J. As, and K. Lischka, *Near UV emission from nonpolar cubic* $Al_xGa_{1-x}N/GaN$ *Quantum Wells*
Appl. Phys. Lett. **89**, 131910 (2006)

10. D.J. As, M. Schnietz, **J. Schörmann**, S. Potthast, J.W. Gerlach, J. Vogt and K. Lischka, *MBE growth of cubic* $Al_xIn_{1-x}N$ *and* $Al_xGa_yIn_{1-x-y}N$ *lattice matched to GaN*
phys. stat. sol. (c) (2006) (accepted)

11. **J. Schörmann**, D.J. As, K. Lischka, P. Schley, R. Goldhahn, S. Li, W. Löffler, M. Hetterich, and H. Kalt, *Molecular Beam Epitaxy of phase pure cubic InN*
Appl. Phys. Lett. **89**, 261903 (2006)

12. **J. Schörmann**, S. Potthast, D.J. As, and K. Lischka, *In situ growth regime characterization of cubic GaN using reflection high energy electron diffraction*
Appl. Phys. Lett. **90**, 041918 (2007)

13. **J. Schörmann**, D.J. As, and K. Lischka, *MBE Growth of cubic InN*
MRS Symp. Proc. Vol. **955E**, I8.3 (2007)

14. S.F. Li, **J. Schörmann**, D.J. As, and K. Lischka, *Room temperature blue and green light emissions from nonpolar cubic InGaN/GaN multi-quantum-wells*

Appl. Phys. Lett. **90**, 071903 (2007)

15. F.Y. Lo, A. Melnikov, D. Reuter, A.D. Wieck, V. Ney, T. Kammermeier, and A. Ney, **J. Schörmann**, S. Potthast, D.J. As, and K. Lischka
Appl. Phys. Lett. (submitted)

16. R. Goldhahn, P. Schley, **J. Schörmann**, D.J. As, K. Lischka, F. Fuchs, F. Bechstedt, C. Cobet, and N. Esser, *Dielectric function and band structure of cubic InN*, Bessy - Annual Report 2006, p. 529 (2007)

Acknowledgement

Firstly, I would like to thank Apl. Prof. Dr. D. J. As. My work was performed under his direct supervision and he has given a lot of valuable advices.

The same gratitude goes to Prof. Dr. K. Lischka who gave me the opportunity to work in this group. Plenty of valuable discussions and advices from him support this challenging work on the research of cubic nitrides.

Thanks also goes to Dr. D. Schikora for his help and discussion about the growth.

Next I have to mention my college, friend and office partner during the last four years, Dr. S. Potthast. I am really sorry that the world best MBE dreamteam will be splitted. I thank him for all the helpful discussions (not only physics) and the after work beers. Specially I have to thank him for playing my taxi driver during my torn ligament.

In addition I would like to thank my other fellow Ph. D. students C. Arens, S. Preuss, Dr. S. Li, Dr. A. Pawlis and especially our ladies E. Tschumak, M. Panfilova and Olga Kasdorf, for the helpful physical and technical discussions.

Of course I am also grateful for the (not only technical) help of our optoelectronics staff, I. Zimmermann, B. Vollmer and S. Igges.

I would like to thank H. Nagasawa and M. Abe from SiC Development Center, HOYA Corporation, for supplying the 3C-SiC substrates.

I have to thank E. A. Decuir Jr. from the University of Arkansas for the collaboration and the nice time during his stay at the University of Paderborn.

I want to thank Dr. A. Khartchenko for his help regarding the X-Ray simulations.

Moreover I have to thank my girl friend Teresa for her love and encouragement she gave me during the last 10 years.

Last but not least I would like to thank my parents for their love, encouragement and financial support during my whole life.